Curvature and shape relaxation in surface-viscous domains

Joseph M. Barakat and Todd M. Squires*
Department of Chemical Engineering, University of California, Santa Barbara, Santa Barbara, California 93106, USA

(Received 6 January 2023; accepted 14 April 2023; published 10 May 2023)

The mechanics of curved, heterogeneous, surfactant-laden surfaces and interfaces are important to a variety of engineering and biological applications. To date, most models of rheologically complex interfaces have focused on homogeneous systems of planar or fixed curvature. In this paper, we investigate a simple, dynamical model of a two-phase surface fluid on a curved interface: a condensed, surface-viscous domain embedded within a surface-inviscid, spherical interface of time-varying radius of curvature. Our aim is to understand how changes in surface curvature generate two-dimensional Stokes flows inside the domain, thereby resisting curvature deformation and distorting the domain shape. We model the surface stress within the domain using the classical Boussinesq-Scriven constitutive equation, simplified for a near-spherical cap undergoing a small-amplitude curvature deformation. We then analyze the frequency-dependent dynamics of the surface stress and curvature within the domain when the pressure difference across the surface is sinusoidally oscillated. We find that the curvature relaxes diffusively, and thus define a Peclet number (Pe) relating the rate of diffusion to the oscillation frequency. At small enough Pe, the surface deforms quasistatically, whereas at high Pe the curvature varies sharply within a thin boundary layer adjacent to the domain border. Consequently, the curvature of the domain appears discontinuous from the rest of the surface under rapid oscillation. We then examine the linear stability of the domain shape to small, nonaxisymmetric perturbations when the surface is steadily compressed (i.e., the pressure difference across it is increased). While the line tension at the domain border tends to maintain circular symmetry, surface-viscous stresses generated by surface compression tend to destabilize the perimeter. A shape instability arises above a critical surface capillary number (Ca) that relates surface-viscous stresses to line tension. Moreover, we show that the mechanism of instability is distinct from that of the famous Saffman-Taylor fingering instability. Various extensions of our model are discussed, including materials with finite dilatational surface viscosity, linear and nonlinear (visco)elasticity, and large-amplitude deformations.

DOI: 10.1103/PhysRevFluids.8.054001

I. INTRODUCTION

The dynamics of curved, heterogeneous, surfactant-laden surfaces and interfaces are important to applications ranging from lung surfactants [1–5] to ultrasound contrast agents [6–10], as well as the basic science of biomembranes [11–13]. Surface heterogeneities naturally emerge as a result of two-dimensional (2D) phase separation, often taking the form of condensed domains embedded in a disordered, continuum fluid [14–16]. The structure, rheology, and dynamics of interfaces with domain heterogeneities have been the subject of investigation for several decades [17–22]. However,

*tsquires@ucsb.edu

the influence of surface curvature, which is highly relevant to applications, is still in the nascent stage of research.

Surface curvature can couple to surface heterogeneity in a number of ways. When the curvature of a surface is suddenly changed, material heterogeneities may deform at a rate different from the rest of the surface due to their dissimilar mechanical properties. Such nonhomogeneous curvature deformations have been observed, for instance, in ultrasonication of lipid-coated microbubbles [9]. Additionally, changes in curvature can lead to surface flows that influence the domain structure and morphology. Examples include the domain-shape instabilities and fingering patterns in Langmuir monolayers of insoluble surfactants [23].

Understanding each of these processes requires a model for the mechanical response of a curved, heterogeneous interface with discontinuous material properties. The simplest mechanical model, the so-called Boussinesq-Scriven constitutive equation [24–26], is applicable to insoluble surfactants compressed to high enough density that they behave as 2D viscous fluids. Most theoretical studies employing the Boussinesq-Scriven model have focused on homogeneous interfaces or planar interfaces of zero curvature [27–30]. However, phase-coexisting surfactant films often exhibit a large mismatch in surface viscosity [21] between the domain (viscous) and the continuum (inviscid) surface phases that is obscured in a homogeneous model. Although recent theoretical work [31–33] has considered the influence of surface curvature on 2D viscous flows, accounting for heterogeneous surface properties remains a challenging and nonlinear problem [34,35].

In this paper, we consider the simplest model for a 2D heterogeneous interface undergoing a uniform curvature deformation: a circular, surface-incompressible domain with surface shear viscosity η_s embedded within a spherical interface, of radius R, that is otherwise compressible and surface inviscid. The curvature of the interface is changed by varying the capillary pressure p across it, and the resulting surface flows in the domain depend upon the rate of compression (or expansion). This simple model aims to elucidate two basic questions: (i) Under what conditions will the curvature of the surface-viscous and surface-inviscid phases relax at different rates, and what parameters govern this relaxation process? (ii) Is the circularly symmetric domain shape linearly stable to surface-viscous flows and, if not, what is the criterion for shape instability?

To simplify the problem of modeling 2D viscous flows within a finite domain of dynamically varying curvature, we consider small-amplitude or quasistatic deformations wherein nonlinear couplings between curvature and flow-induced surface stresses may be neglected. We also neglect couplings to bulk fluid flows so the problem is entirely 2D. Thus, our model of 2D fluid domains is somewhat analogous to models of three-dimensional (3D) droplets in Stokes flows, albeit with important differences arising from the curvature of the (non-Euclidean) manifold. The aforementioned simplifications enable analytical progress in modeling the relaxation dynamics of domain curvature and shape in response to a time-dependent pressure forcing, which would otherwise require a purely numerical treatment. As we will show, our semianalytical model will reveal useful timescales for these relaxation processes that encode a competition between thermodynamic (i.e., equilibrium) and hydrodynamic (nonequilibrium) driving forces.

The remainder of this paper is organized as follows. In Sec. II, we present the relevant continuum-mechanical theory for describing the linear dynamics of a 2D surface-viscous domain on a spherical interface of evolving curvature. We then apply this theory in Sec. III to describe (Sec. III A) axisymmetric deformations as a function of the rate of compression, and (Sec. III B) nonaxisymmetric shape instabilities under slow compression rates. A discussion of our results and possible extensions of our model is given in Sec. IV. Concluding remarks are given in Sec. V.

II. THEORY

Figure 1 sketches the geometry of a surface-viscous domain embedded in a spherical, surface-inviscid surface. In the forthcoming theoretical development, it will be useful to think of the domain as the 2D analog of a 3D droplet. When placed under a static capillary pressure p_0, the domain is

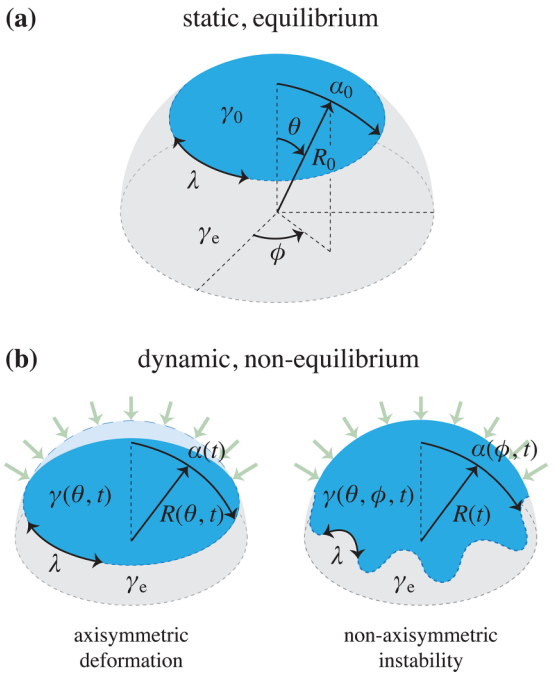

FIG. 1. Schematic of a surface-viscous, 2D domain on a surface-inviscid, spherical surface. (a) At equilibrium, the domain adopts a static cap angle α_0 and radius of curvature R_0 according to Eqs. (1) and (2). (b) When the surface is dynamically compressed, surface-viscous stresses can induce an axisymmetric curvature deformation (left) or a nonaxisymmetric shape instability (right).

shaped into a spherical cap with radius of curvature R_0 according to the Young-Laplace law,

$$\frac{2\gamma_0}{R_0} = p_0, \tag{1}$$

where γ_0 is the static surface tension *inside* the domain [see Fig. 1(a)]. The tension *outside* the domain, denoted by γ_e, is in general not equal to γ_0. Any line tension λ at the domain edge results in a mismatch in equilibrium tension (and curvature) between the surface-viscous and surface-inviscid phases. For small line tensions $\lambda \ll \gamma_0 R_0$, a balance of stresses at the edge of the cap yields the auxiliary constraint,

$$\gamma_0 = \gamma_e - \frac{\lambda}{R_0 \tan\alpha_0}, \tag{2}$$

where α_0 is the static cap angle that reflects the characteristic size of the domain. Equation (2) expresses the mismatch in surface tension that compensates for a small, but non-negligible, line tension at the border of the domain. It is the 2D analog of the Young-Laplace law [Eq. (1)], which relates the capillary pressure across a surface to the surface tension. Taken together, Eqs. (1) and (2) completely specify the equilibrium statics of the domain.

Varying the pressure $p(t)$ as a function of time t results in a *dynamic* surface tension $\gamma(\theta,\phi,t)$ and radius $R(\theta,\phi,t)$ that depend upon the colatitude θ and azimuth ϕ of the unperturbed spherical cap [Fig. 1(b)]. If the pressurization is sufficiently weak (i.e., p is close to p_0), then the curvature of the perturbed surface is governed by the linear differential equation,

$$\frac{2\gamma}{R_0} - \gamma_0\left(\nabla_s^2 R + \frac{2R}{R_0^2}\right) = p - p_0, \tag{3}$$

where $\nabla_s \equiv (\hat{\boldsymbol{e}}_\theta/R_0)(\partial/\partial\theta) + (\hat{\boldsymbol{e}}_\phi/R_0 \sin\theta)(\partial/\partial\phi)$ is the surface gradient on the unperturbed sphere and $\nabla_s^2 \equiv \nabla_s \cdot \nabla_s$ is the associated surface Laplacian [36]. In addition to perturbing the shape, the pressure forcing also produces an incompressible surface Stokes flow $\boldsymbol{v}_s = v_\theta \hat{\boldsymbol{e}}_\theta + v_\phi \hat{\boldsymbol{e}}_\phi$. Conservation of mass on a dilating spherical surface requires that

$$\nabla_s \cdot \boldsymbol{v}_s + \frac{2}{R_0}\frac{\partial R}{\partial t} = 0. \tag{4}$$

This surface flow generates an anisotropic surface stress tensor $\boldsymbol{\sigma}_s$ that is work conjugate to the surface velocity-gradient tensor $\nabla_s \boldsymbol{v}_s$. We model the domain as a 2D incompressible, surface-viscous fluid with surface shear viscosity η_s, whose the surface stresses are given by the Boussinesq-Scriven constitutive law [24–26],

$$\boldsymbol{\sigma}_s = \gamma \boldsymbol{\delta}_s + \eta_s[(\nabla_s \boldsymbol{v}_s) \cdot \boldsymbol{\delta}_s + \boldsymbol{\delta}_s \cdot (\nabla_s \boldsymbol{v}_s)^\top - (\nabla_s \cdot \boldsymbol{v}_s)\boldsymbol{\delta}_s], \tag{5}$$

where $\boldsymbol{\delta}_s \equiv \hat{\boldsymbol{e}}_\theta \hat{\boldsymbol{e}}_\theta + \hat{\boldsymbol{e}}_\phi \hat{\boldsymbol{e}}_\phi$ is the unit tensor on the sphere. Momentum conservation then requires that

$$\boldsymbol{\delta}_s \cdot (\nabla_s \cdot \boldsymbol{\sigma}_s) = \nabla_s \gamma + \eta_s \boldsymbol{\delta}_s \cdot \left(\nabla_s^2 \boldsymbol{v}_s + \frac{2\boldsymbol{v}_s}{R_0^2}\right) = \boldsymbol{0}, \tag{6}$$

which is the 2D analog of the Stokes equation of motion. The first two terms on the right-hand side of Eq. (6) bear obvious resemblance to the hydrodynamic pressure gradient and viscous momentum flux in 3D Stokes flow. The last term reflects the extra momentum flux due to the finite Gaussian curvature of the surface, $1/R_0^2$ [31].

In Eqs. (3) and (6), it is tacitly assumed that the only stress exerted by the 3D bulk phase onto the 2D surface-viscous domain is a dynamic pressure $p(t)$. In doing so, we have neglected hydrodynamic stresses associated with bulk fluid flow, which are proportional to a bulk shear viscosity η (or, more generally, a bulk viscoelasticity). The relative importance of surface stresses and bulk stresses is captured by the Boussinesq number, $\mathrm{Bq} = \eta_s/\eta L$, where L is a length scale over which the flow decays in the third dimension [37]. (For spherical surfaces of high curvature, this length scale is given by the sphere radius R_0 due to screening of the bulk fluid flow [13,31,38].) We assume that Eq. (6) is approximately valid so long as $\mathrm{Bq} \gg 1$. Additionally, it should be noted that the surface tension γ appearing in Eqs. (5) and (6) is a Lagrange field that ensures satisfaction of the surface incompressibility condition [Eq. (4)], and thus plays a similar role to the pressure in 3D viscous flows. For surface incompressibility to hold, the area-compression modulus E_s of the surface-viscous phase must be large compared to the characteristic surface-viscous stress $\eta_s V/R_0\alpha_0$, where V is the velocity of the inter-phase boundary. In terms of a dimensionless Marangoni number, $\mathrm{Ma} = E_s R_0 \alpha_0/\eta_s V$, this condition requires that $\mathrm{Ma} \gg 1$ [28,39,40].

As the pressure oscillates, the shape of the 2D domain is allowed to deform. Hence, the preceding equations must be solved subject to free-boundary conditions at the edge of the domain [i.e., at $\theta = \alpha(\phi, t)$]. These boundary conditions are similar to those used to specify the shape of 3D droplets deforming in Stokes flows [41]. First, mechanical equilibrium requires that the surface stresses balance at the edge [42]. Letting $\boldsymbol{r}(\phi, t) = R_0 \hat{\boldsymbol{e}}_r|_{\theta=\alpha(\phi,t)}$ define the radial position along the boundary, this condition reads

$$\hat{\boldsymbol{n}} \cdot \boldsymbol{\sigma}_s = \gamma_e \hat{\boldsymbol{n}} + \lambda\left(\frac{\partial \hat{\boldsymbol{t}}}{\partial s} - \hat{\boldsymbol{t}} \times \frac{\hat{\boldsymbol{e}}_\theta}{R_0}\right) \quad \text{at} \quad \theta = \alpha(\phi, t), \tag{7}$$

where $ds = |\partial \boldsymbol{r}/\partial\phi|\, d\phi$ is the differential arc length, $\hat{\boldsymbol{t}} = \partial \boldsymbol{r}/\partial s$ is the unit tangent, and $\hat{\boldsymbol{n}} = \hat{\boldsymbol{t}} \times \hat{\boldsymbol{e}}_r$ is the unit normal. Equation (7) is the dynamic version of the static stress condition, Eq. (2). The components of Eq. (7) parallel to $\hat{\boldsymbol{n}}$ and $\hat{\boldsymbol{t}}$ are the 2D analogs of the familiar normal and shear stress boundary conditions for 3D droplets. The transverse component, parallel to $\hat{\boldsymbol{e}}_r$, has no analog in 3D. This latter condition ensures that the shape of the surface is continuous and smooth in crossing the boundary between the surface-viscous and surface-inviscid phases. Smoothness is required because

the surface stresses, modeled by Eq. (5), do not contain a transverse component (unlike curved shells of finite thickness, which exhibit transverse shear stresses due to their bending stiffness).

In addition to the surface stress balance, the velocity of the boundary must evolve with the local flow field according to the kinematic condition,

$$\frac{\partial \alpha}{\partial t} = \boldsymbol{v}_s \cdot \boldsymbol{\nabla}_s(\theta - \alpha) \quad \text{at} \quad \theta = \alpha(\phi, t), \tag{8}$$

subject to the constraint that the total surface area inside the domain remains conserved. The latter constraint is obtained by integrating the continuity equation [Eq. (4)] over the surface of the domain.

Taken together, Eqs. (3)–(8) now form a closed system that may be directly integrated to calculate the domain shape, curvature, surface velocities, and surface stresses. The time evolution of these dynamic variables depends upon the geometric properties (R_0, α_0) and material properties (η_s, γ_0, λ) of the surface-viscous domain. In particular, it may be shown (see Appendix A) using Eqs. (3), (4), and (6) that the surface tension and curvature obey the surface diffusion equations,

$$\left(\frac{\partial}{\partial t} - D\nabla_s^2\right)\gamma = \frac{R_0 \dot{p}}{2}, \tag{9}$$

$$\left(\frac{\partial}{\partial t} - D\nabla_s^2\right)\left(\nabla_s^2 R + \frac{2R}{R_0^2}\right) = 0, \tag{10}$$

where $\dot{p} \equiv dp/dt$ and

$$D = \frac{\gamma_0 R_0^2}{4\eta_s} \tag{11}$$

is a diffusion coefficient. Although Eqs. (9) and (10) appear to independently govern the evolution of γ and $\nabla_s^2 R + 2R/R_0^2$, respectively, the two are, in fact, coupled through the boundary conditions, Eqs. (7) and (8).

Equations (9) and (10) reveal a timescale,

$$\tau_D \equiv \frac{(R_0\alpha_0)^2}{D} = \frac{4\eta_s \alpha_0^2}{\gamma_0}, \tag{12}$$

for surface stress and curvature to diffuse a distance $R_0\alpha_0$ across a spherical surface. The boundary equations [Eqs. (7) and (8)] similarly govern the time evolution of the dynamic cap angle, with a characteristic boundary velocity,

$$V = \frac{\lambda}{\eta_s}, \tag{13}$$

determined by balancing surface-viscous and line-tension forces. This gives a second timescale,

$$\tau_V \equiv \frac{R_0\alpha_0}{V} = \frac{\eta_s R_0 \alpha_0}{\lambda}, \tag{14}$$

over which boundary distortions can relax. Thus, even before pursuing a detailed solution of the aforementioned equations, Eqs. (12) and (14) provide a great deal of physical insight into the relevant relaxation processes and their associated time scales. Quantitative estimates of these timescales for a prototypical surfactant system are delayed until Sec. IV but, for most physical systems of relevance, $\tau_D \ll \tau_V$. The comparison of these timescales to the characteristic rate of deformation determines which forces (surface viscosity, surface tension, or line tension) dominate the dynamics.

Unfortunately, pursuing a detailed solution for an arbitrary domain shape is complicated by the free-boundary conditions [Eqs. (7) and (8)], which are highly nonlinear. To simplify the analysis, we will first consider a reference base shape with axial symmetry so the flow problem may be solved as a function of the colatitude on the sphere (Sec. III A). Subsequently, the linear stability

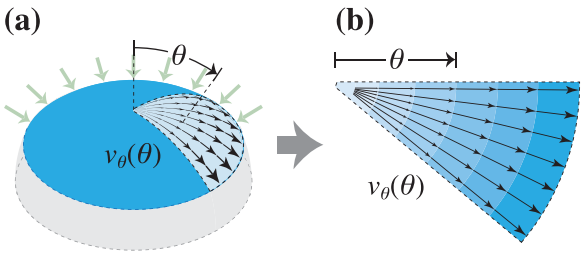

FIG. 2. Axisymmetric dilatation of a surface-incompressible, spherical cap induces surface shear. (a) Compression of the surface induces an axisymmetric surface flow $v_\theta(\theta)$ that accelerates along the colatitude θ. (b) A planar projection reveals that material elements are stretched by the flow.

of this base shape against small, nonaxisymmetric distortions will be tested (Sec. III B). The latter analysis will reveal a critical deformation rate above which the symmetric domain shape becomes unstable.

III. RESULTS

A. Axisymmetric deformations

As a first approximation, we assume that the domain maintains circular symmetry with a dynamic cap angle $\alpha(t)$ that is constant along the azimuth ϕ [see Fig. 1(b), *left*]. Thus, the surface velocity v_θ, surface tension γ, and radius R must be determined as a function of the colatitude θ and time t. Even in the axisymmetric case, the surface flow that results from changing the capillary pressure across the surface can induce surface shear stress. Figure 2 clarifies this effect. When a spherical surface is compressed, its metric changes and induces a flow v_θ that varies along θ to preserve surface incompressibility [see Eq. (4)]. The shear rates $(1/R_0)(\partial v_\theta/\partial\theta)$ and $(v_\theta/R_0)\cot\theta$ associated with this flow stretch material elements along the colatitude on the sphere without changing their surface area. These, in turn, produce anisotropic surface stresses proportional to the surface shear viscosity η_s.

Our objective is to understand how these flows produced by compression or expansion of the surface affect the evolution of surface stress and curvature in the surface-viscous domain, focusing only on circularly symmetric domains for the time being. To probe the temporal dynamics, we assume a sinusoidal pressure perturbation,

$$p(t) = p_0 + \delta p e^{i\omega t}, \tag{15}$$

where p_0 is the static pressure [given by Eq. (1)], ω is the angular frequency, and δp is the amplitude of the pressure perturbation. Hence, the time evolution of the system is determined by a competition between the probing frequency ω and the relaxation time scales τ_D and τ_V given, respectively, by Eqs. (12) and (14). For the sake of simplicity, we shall focus on the regime where $\tau_D \ll \tau_V$ and, in so doing, neglect the role of line tension in our analysis of axisymmetric deformations. This simplification is justified provided that $\lambda \ll \gamma_0 R_0$, as was assumed in Eqs. (2) and (7).

With line tension neglected, the only relevant timescale in the problem is the diffusive timescale τ_D. The ratio of the probing frequency ω to the rate of diffusion R_0^2/D defines a Peclet number,

$$\mathrm{Pe} \equiv \frac{\omega R_0^2}{D} = \frac{4\omega\eta_s}{\gamma_0}, \tag{16}$$

in which the dependence on the surface-shear viscosity η_s and static surface tension γ_0 clearly emerges. We have avoided calling the dimensionless quantity in Eq. (16) the capillary number, and this choice of nomenclature merits some justification. In 3D Stokes flows within and around

deforming droplets, the capillary number reflects the ratio of viscous stresses, which tend to distort a droplet's shape, to surface tension, which penalizes shape deformation. The natural 2D analog would, therefore, be the ratio of surface-viscous stresses to line tension, the latter of which we have neglected here. By contrast, Eq. (16) expresses the competition between surface-viscous stresses and surface tension in distorting the *curvature* of a 2D domain, which has no analog in 3D. The choice of naming this quantity the Peclet number is motivated by the observation that the curvature relaxes diffusively. In Sec. III B, we shall revisit the role of the line tension in the low-frequency limit (Pe $\to$ 0) wherein the slow timescale τ_V can no longer be ignored. In this regime, a surface capillary number [denoted by Ca, see Eq. (38)] naturally emerges.

The forthcoming analysis will be carried out in the linear-response limit, for which the pressure amplitude $\delta p \ll p_0$. Neglecting initial transient effects, the dynamical variables eventually achieve a periodic steady state with fundamental frequency ω,

$$v_\theta(\theta, t) = \delta v_\theta(\theta) e^{i\omega t}, \tag{17}$$

$$\gamma(\theta, t) = \gamma_0 + \delta\gamma(\theta) e^{i\omega t}, \tag{18}$$

$$R(\theta, t) = R_0 + \delta R(\theta) e^{i\omega t}, \tag{19}$$

$$\alpha(t) = \alpha_0 + \delta\alpha e^{i\omega t}, \tag{20}$$

neglecting the higher harmonics corresponding to integer multiples of ω. Rendering the linear-response functions dimensionless as $\delta\bar{p} = \delta p/p_0$, $\delta\bar{v}_\theta = \delta v_\theta/(i\omega R_0)$, $\delta\bar{\gamma} = \delta\gamma/\gamma_0$, and $\delta\bar{R} = \delta R/R_0$ and taking the finite Fourier transform of Eqs. (3)–(6) leads to a system of ordinary differential equations,

$$\frac{d^2\delta\bar{R}}{d\theta^2} + \cot\theta \frac{d\delta\bar{R}}{d\theta} + 2\delta\bar{R} - 2\delta\bar{\gamma} = -2\delta\bar{p}, \tag{21}$$

$$\frac{d\delta\bar{v}_\theta}{d\theta} + \delta\bar{v}_\theta \cot\theta + 2\delta\bar{R} = 0, \tag{22}$$

$$\frac{d^2\delta\bar{v}_\theta}{d\theta^2} + \cot\theta \frac{d\delta\bar{v}_\theta}{d\theta} + (1 - \cot^2\theta)\delta\bar{v}_\theta + \frac{4}{i\mathrm{Pe}} \frac{d\delta\bar{\gamma}}{d\theta} = 0, \tag{23}$$

subject to symmetry conditions at the centerline,

$$\delta\bar{v}_\theta = 0, \quad \frac{d\delta\bar{\gamma}}{d\theta} = 0, \quad \frac{d\delta\bar{R}}{d\theta} = 0 \quad \text{at} \quad \theta = 0, \tag{24}$$

the surface stress conditions [Eq. (7) with $\lambda/\gamma_0 R = 0$],

$$\frac{d\delta\bar{R}}{d\theta} = 0, \quad \frac{d\delta\bar{v}_\theta}{d\theta} - \delta\bar{v}_\theta \cot\theta + \frac{4}{i\mathrm{Pe}}\delta\bar{\gamma} = 0 \quad \text{at} \quad \theta = \alpha_0, \tag{25}$$

and the kinematic condition [Eq. (8)],

$$\delta\bar{v}_\theta = \delta\alpha \quad \text{at} \quad \theta = \alpha_0. \tag{26}$$

The source that drives the system out of equilibrium is the pressure perturbation on the right-hand side of Eq. (21). The Peclet number Pe, defined by Eq. (16), appears in Eqs. (23) and (25) and reflects the strength of surface-viscous stresses relative to the static tension in the domain. Two corollaries may be derived from the above equations via integration over the cap surface. First, multiplying the incompressibility condition [Eq. (22)] by $2\pi \sin\theta\, d\theta$, integrating from $\theta = 0$ to α_0, and applying the kinematic condition [Eq. (26)] yields a global condition conserving the total surface area inside the domain:

$$\int_0^{\alpha_0} 2\delta\bar{R} \sin\theta\, d\theta + \delta\alpha \sin\alpha_0 = 0. \tag{27}$$

This condition relates the radial displacement $\delta\bar{R}$ to the perturbation of the cap angle $\delta\alpha$. Second, integrating the momentum balance equations [Eqs. (21) and (23)] over the cap surface and applying the surface stress condition [Eq. (25)] yields a boundary condition for the radial displacement:

$$\delta\bar{R} = -\delta\bar{p} \quad \text{at} \quad \theta = \alpha_0. \tag{28}$$

This condition, which is necessary to conserve forces globally, ensures that the surface is continuous across the interphase boundary.

We have numerically solved Eqs. (21)–(28) for various values of Pe and the initial cap angle α_0 using standard methods for one-dimensional boundary-value problems [43]. Below, we consider the two limiting cases in which Pe is asymptotically small or large to gain analytical insight into the structure of the solutions.

As the frequency tends to zero (Pe $\to$ 0), the rate of deformation is so slow that the domain deforms isotropically. Equation (21) is then satisfied by the trivial solution $\delta\bar{R} = -\delta\bar{p}$ and $\delta\bar{\gamma} = 0$–i.e., the radius of curvature of the domain shrinks with increasing pressure while the surface tension remains essentially unchanged. However, if the probing frequency ω is finite but much smaller than the diffusive frequency $2\pi/\tau_D$ [i.e., Pe $\ll 2\pi/\alpha_0^2$ using Eq. (12)], then surface-viscous stresses weakly distort the curvature of the 2D domain. A small-Pe regular perturbation analysis of Eqs. (21)–(28) furnishes the following asymptotic expansions for the linear-response functions:

$$\frac{\delta\bar{v}_\theta(\theta)}{\delta\bar{p}} = 2\tan\left(\frac{1}{2}\theta\right) + O(\mathrm{Pe}), \tag{29}$$

$$\frac{\delta\bar{\gamma}(\theta)}{\delta\bar{p}} = i\mathrm{Pe}\left[\ln\left(\frac{1+\cos\theta}{1+\cos\alpha_0}\right) - \frac{1}{2}\tan^2\left(\frac{1}{2}\alpha_0\right)\right] + O(\mathrm{Pe}^2), \tag{30}$$

$$\frac{\delta\bar{R}(\theta)}{\delta\bar{p}} = -1 + i\mathrm{Pe}\left[\ln\left(\frac{1+\cos\theta}{1+\cos\alpha_0}\right) + \frac{\cos\alpha_0 - \cos\theta}{1+\cos\alpha_0}\right] + O(\mathrm{Pe}^2). \tag{31}$$

Thus, the dilatation of the surface metric produces an $O(1)$ axisymmetric flow [Eq. (29)] that, in turn, generates surface-viscous shear stresses. These stresses contribute the $O(\mathrm{Pe})$ corrections to Eqs. (30) and (31) that drive the surface tension and curvature out of equilibrium.

At much faster oscillation frequencies (Pe $\gg 2\pi/\alpha_0^2$), the deformation rate is too rapid for the surface tension and curvature to relax on a commensurate timescale. Consequently, the surface-viscous domain retains its initial curvature $1/R_0$ and undergoes a rigid-body translation as the pressure oscillates (with amplitude $\delta\bar{R} = -\delta\bar{p}\cos\theta/\cos\alpha_0$), while the tension oscillates uniformly (with amplitude $\delta\bar{\gamma} = \delta\bar{p}$) in order to offset the Laplace pressure. However, this translating-spherical-cap solution fails to satisfy the edge boundary conditions [Eqs. (25) and (26)], which require that the profile of the surface-viscous domain smoothly connects to the embedding, surface-inviscid phase on the rest of the sphere. Resolving this apparent discrepancy requires the application of singular perturbation theory, which reveals that a rapid variation in surface curvature over an $O(\mathrm{Pe}^{-\frac{1}{2}})$ diffusive boundary layer (near $\theta = \alpha_0$) is facilitated by an $O(\mathrm{Pe}^{\frac{1}{2}})$ change in surface tension (see Fig. 3). Analysis within the boundary layer furnishes the following large-Pe singular perturbation expansions (derived in Appendix B):

$$\frac{\delta\bar{v}_\theta(\theta)}{\delta\bar{p}} = \frac{\sin\theta}{\cos\alpha_0}[1 - (i\mathrm{Pe})^{-\frac{1}{2}}\tan\alpha_0] + O(\mathrm{Pe}^{-1}), \tag{32}$$

$$\frac{\delta\bar{\gamma}(\theta)}{\delta\bar{p}} = 1 - \frac{1}{2}(i\mathrm{Pe})^{\frac{1}{2}}\tan\alpha_0\exp[(i\mathrm{Pe})^{\frac{1}{2}}(\theta-\alpha_0)] + O(\mathrm{Pe}^{-\frac{1}{2}}), \tag{33}$$

$$\frac{\delta\bar{R}(\theta)}{\delta\bar{p}} = -\frac{\cos\theta}{\cos\alpha_0}[1 - (i\mathrm{Pe})^{-\frac{1}{2}}\tan\alpha_0] - (i\mathrm{Pe})^{-\frac{1}{2}}\tan\alpha_0\exp[(i\mathrm{Pe})^{\frac{1}{2}}(\theta-\alpha_0)] + O(\mathrm{Pe}^{-1}). \tag{34}$$

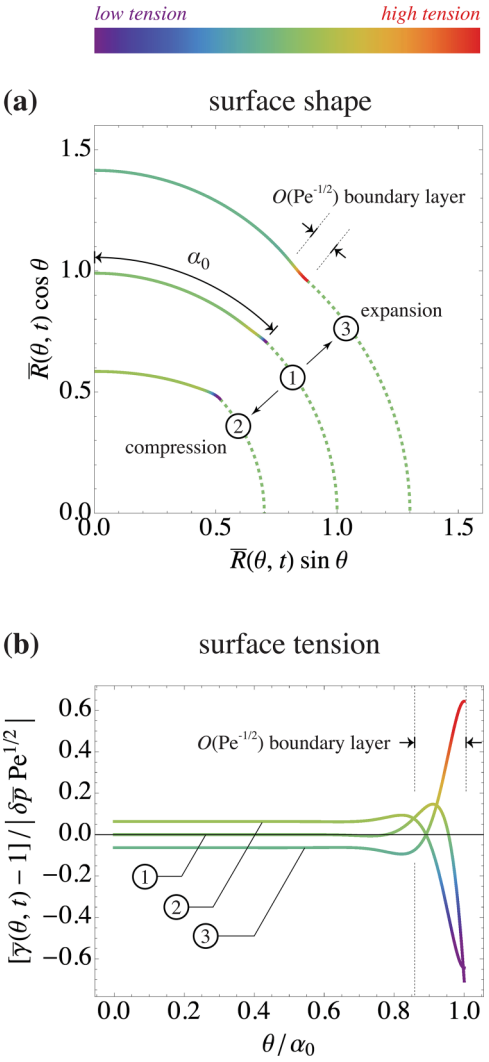

FIG. 3. (a) Surface shape and (b) surface tension within the surface-viscous cap at high Peclet number ($\mathrm{Pe} = 10^3$), cap angle $\alpha_0 = \pi/4$, and pressure amplitude $\delta\bar{p} = 30\%$ [see Eqs. (33) and (34)]. Three different time points are shown for (1) the unperturbed surface, (2) maximum compression, and (3) maximum expansion. Colors in (a), (b) indicate the magnitude of the surface tension.

The agreement between these asymptotic solutions and the numerical solution of Eqs. (21)–(28) is excellent so long as $\alpha_0 < \pi/2$. Figure 3 plots the asymptotic solutions [Eqs. (33) and (34)] for $\mathrm{Pe} = 10^3$ and $\alpha_0 = \pi/4$; a large amplitude $\delta\bar{p} = 30\%$ (beyond the linear-response limit) is shown to exaggerate the changes in curvature and tension that result from a change in pressure. The plots reveal the exponential variation within the boundary layer in order to satisfy the surface-stress condition at the domain edge.

The preceding analysis shows that surface-viscous stresses resist the curvature deformation that would result from a change in pressure. When these stresses become appreciably large (i.e., at ultrafast driving frequencies or $\mathrm{Pe} \to \infty$), then the initial curvature $1/R_0$ of the spherical cap remains unchanged as the domain undergoes a rigid-body motion. At these frequencies, the tension remains nearly uniform (except near the boundary layer) and oscillates synchronously with the

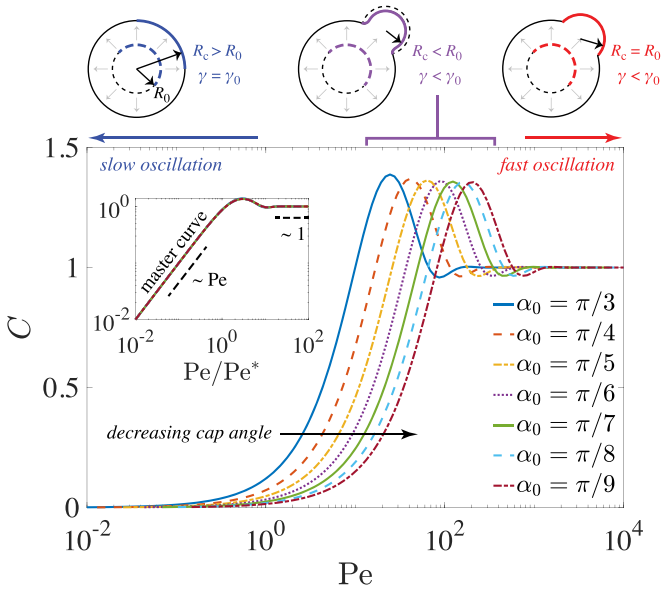

FIG. 4. The constant C [defined by Eq. (35)] gauges the deviation from the equilibrium tension and exhibits a nonmonotonic dependence on the Peclet number Pe. Main: Plots of C against Pe for various cap angles α_0. At small Pe, the domain curvature deforms isotropically with small variation in tension [$\sim O(\mathrm{Pe})$]. At large Pe, the tension varies [$\sim O(1)$] while the curvature remains fixed. Inset: Plots collapse onto a master curve when plotted against the ratio $\mathrm{Pe}/\mathrm{Pe}^*$ [see Eq. (36)]. The maximum change in tension occurs at $\mathrm{Pe}/\mathrm{Pe}^* \approx 3$. Top: Pictures depict the change in the radius of curvature R_c and surface tension γ that result from oscillating the pressure at various frequencies (i.e., Peclet numbers).

pressure as $\gamma(t)/\gamma_0 = p(t)/p_0$ [see Fig. 3(b)]. On the other hand, a gentle forcing ($\mathrm{Pe} \to 0$) causes the curvature to freely oscillate while the tension remains essentially unchanged. Thus, there is a tradeoff between curvature and tension as the frequency is increased. This tradeoff is clearly represented in the normal momentum balance [Eq. (21)], which relates the surface tension perturbation $\delta\gamma$ to the curvature perturbation $\nabla_s^2 \delta R + 2\delta R/R_0^2$.

Since the curvature and tension are inextricably linked, we define the relative change in tension at the centerline ($\theta = 0$),

$$C \equiv \left| \frac{\delta\bar{\gamma}(0)}{\delta\bar{p}} \right|, \tag{35}$$

as a gauge for the departure from equilibrium statics. When $C = 0$, then the domain deforms quasistatically with equilibrium tension γ_0, whereas for $C > 0$ excess surface-viscous stresses contribute to the dynamic tension. Figure 4 plots our numerical computations of C against the Peclet number Pe for various cap angles α_0. The pictures shown above the plots depict the change in the domain curvature $1/R_c$ that accompanies a change in tension. As expected from our previous arguments, C varies from 0 (when $\gamma/\gamma_0 = 1$ and $R_0/R_c = p/p_0$) to 1 ($\gamma/\gamma_0 = p/p_0$ and $R_0/R_c = 1$) as Pe is increased. Interestingly, we also find that C passes through a maximum at an intermediate value of the Peclet number (the exact value decreases with the cap angle as $\sim\alpha_0^{-2}$). This maximum reflects the crossover frequency at which surface tension and viscous stresses balance within the domain. Using our asymptotic expansions for the surface tension perturbation [Eqs. (30) and (33)], we estimate the crossover Peclet number to be

$$\mathrm{Pe}^* = \left\{ \ln\left[\sec^2\left(\tfrac{1}{2}\alpha_0\right)\right] - \tfrac{1}{2}\tan^2\left(\tfrac{1}{2}\alpha_0\right) \right\}^{-1}, \tag{36}$$

which varies like $\sim 8/\alpha_0^2$ as $\alpha_0 \to 0$. Plotting C against the ratio $\mathrm{Pe}/\mathrm{Pe}^*$ collapses all of the numerical data onto a master curve (Fig. 4, inset), with a maximum ≈ 1.36 found at $\mathrm{Pe}/\mathrm{Pe}^* \approx 3$. Physically, this maximum reflects a roughly 36% increase in the amplitude, above that predicted by equilibrium statics and due entirely to extra surface-viscous stresses.

We conclude this section by briefly discussing potential nonlinear effects that are not included in our linear-response model for the coupled evolution of curvature and tension in surface-viscous domains. Under fast compression [see label (2) in Fig. 3], the tension at the domain edge ($\theta = \alpha_0$) can become very large and negative, even if the pressure amplitude is relatively small. [Indeed, inspection of Eq. (33) reveals an $O(\mathrm{Pe}^{\frac{1}{2}})$ contribution to the tension through the boundary layer that can easily overwhelm the static tension.] Negative surface tensions $\gamma < 0$ are responsible for wrinkling and buckling instabilities in viscous films [44–47] and elastic sheets [48,49] due to nonlinear tension-curvature couplings that are neglected in the linearized Eq. (3). Physically, a continuum surface under negative tension is unable to support a capillary pressure, driving out-of-plane surface undulations. Resisting this driving force is the bending stiffness of the surface [also neglected in Eq. (3)], which limits the wavelength of the undulations [48]. The possibility of out-of-plane, nonaxisymmetric shape instabilities driven by high-frequency, surface-viscous shearing forces represents an interesting extension of our purely axisymmetric, linearized model and merits future investigation. In the next section, we consider a different type of nonaxisymmetric shape instability that is confined to the plane of the surface and relevant to low frequencies.

B. Nonaxisymmetric instability

Our analysis of axisymmetric deformations revealed the competition between surface-viscous stresses and surface tension that determines the resistance to changes in curvature. There is an obvious problem, however, with the presumption of axisymmetry, because the surface flows resulting from a change in capillary pressure could potentially destabilize the domain perimeter. The only force preserving the circular symmetry of the domain is the line tension λ, which was neglected in Sec. III A. The critical compression rate above which axisymmetry is broken must, therefore, depend in some way upon the ratio $\lambda/(\eta_s R_0)$ between the line-tension force and the surface-viscous shearing force. In this section, we will determine this critical condition via a linear stability analysis (for a schematic of the nonaxisymmetric problem, see Fig. 1(b), *right*).

The base state for our analysis, about which we wish to perturb, is the axisymmetric solution presented in the previous section. Generally speaking, this base state oscillates periodically in time and could be analyzed using Floquet theory [50,51]. In lieu of studying the periodic problem in full detail, a great deal of insight may be gleaned by focusing only on a quasisteady increase in the capillary pressure,

$$\frac{dp}{dt} \equiv \dot{p} = \epsilon p_0, \tag{37}$$

where $\epsilon > 0$ is the rate of compression. (The analogous calculation under expansion is given by $\epsilon < 0$.) In this way, ϵ replaces the frequency ω of the previous section as the relevant rate scale. We shall further restrict our attention to deformation rates much slower than the rate of surface diffusion, $\epsilon \ll \tau_D^{-1}$, so that $\tau_V (\gg \tau_D)$ becomes the relevant relaxation timescale [see Eq. (14)]. The ratio between ϵ and the characteristic rate of shape relaxation V/R_0 defines a surface capillary number,

$$\mathrm{Ca} \equiv \frac{\epsilon R_0}{V} = \frac{\epsilon \eta_s R_0}{\lambda}, \tag{38}$$

which will later be shown to determine the onset of a shape instability.

Our focus on slow, quasistatic compressions can also be regarded as the limit of vanishingly small oscillation frequencies (i.e., $\mathrm{Pe} \to 0$). In this regime, surface diffusion occurs rapidly and the

acceleration of the surface is negligible by comparison. Thus, Eqs. (29)–(31) may be applied to determine the kinematics and stresses of the base state. Taking Pe $\to$ 0, Eq. (31) defines a steady, uniform contraction of the surface:

$$\frac{dR}{dt} \equiv \dot{R} = -\epsilon R_0. \tag{39}$$

This deformation, in turn, induces an axisymmetric base flow [Eq. (29)],

$$v_\theta(\theta) = 2\epsilon R_0 \tan\left(\tfrac{1}{2}\theta\right), \tag{40}$$

and, by surface incompressibility, a nonuniform surface tension [Eq. (30)],

$$\gamma(\theta) = \gamma_0 + 4\epsilon\eta_s\left[\ln\left(\frac{1+\cos\theta}{1+\cos\alpha}\right) - \frac{1}{2}\tan^2\left(\frac{1}{2}\alpha\right)\right]. \tag{41}$$

Here, the parametric dependence on time through $\alpha(t)$ has been suppressed for clarity. Using Eq. (40) and the kinematic condition [Eq. (8)], the dynamic cap angle evolves according to

$$\frac{d\alpha}{dt} \equiv \dot{\alpha} = 2\epsilon \tan\left(\frac{1}{2}\alpha\right). \tag{42}$$

Given this quasisteady, axisymmetric base state, we may now analyze its stability by perturbing the dynamic cap angle as

$$\alpha \to \alpha(t) + \delta\alpha(\phi, t), \tag{43}$$

while holding fixed the rate of contraction:

$$\delta\dot{R} = 0. \tag{44}$$

Thus, the evolving curvature of the surface remains unperturbed. However, the shape distortion induces a nonaxisymmetric perturbation to the surface velocities and stresses:

$$\boldsymbol{v}_s \to v_\theta(\theta)\,\hat{\boldsymbol{e}}_\theta + \delta\boldsymbol{v}_s(\theta, \phi, t), \tag{45}$$

$$\gamma \to \gamma(\theta) + \delta\gamma(\theta, \phi, t), \tag{46}$$

where the axisymmetric base functions $v_\theta(\theta)$ and $\gamma(\theta)$ are given by Eqs. (40) and (41). Fluid incompressibility ensures that the shape distortion is area preserving and, therefore, the perturbation flow is purely solenoidal,

$$\boldsymbol{\nabla}_s \cdot \delta\boldsymbol{v}_s = 0, \tag{47}$$

which follows from Eqs. (4), (44), and (45). Thus, the velocity perturbation is completely described by a surface stream function $\delta\psi(\theta, \phi, t)$, defined by

$$\delta\boldsymbol{v}_s = -\boldsymbol{\nabla}_s \times (\delta\psi\hat{\boldsymbol{e}}_r), \tag{48}$$

or, in component form,

$$\delta v_\theta = -\frac{\csc\theta}{R_0}\frac{\partial\delta\psi}{\partial\phi}, \quad \delta v_\phi = \frac{1}{R_0}\frac{\partial\delta\psi}{\partial\theta}, \tag{49}$$

which automatically satisfies Eq. (47). Taking the surface curl and surface divergence of the momentum equation [Eq. (6)] yields a set of coupled differential equations for the stream function and surface tension perturbations:

$$\left(\frac{\partial^2}{\partial\theta^2} + \cot\theta\frac{\partial}{\partial\theta} + \csc^2\theta\frac{\partial^2}{\partial\phi^2}\right)\left(\frac{\partial^2\delta\psi}{\partial\theta^2} + \cot\theta\frac{\partial\delta\psi}{\partial\theta} + \csc^2\theta\frac{\partial^2\delta\psi}{\partial\phi^2} + 2\delta\psi\right) = 0, \tag{50}$$

$$\frac{\partial^2\delta\gamma}{\partial\theta^2} + \cot\theta\frac{\partial\delta\gamma}{\partial\theta} + \csc^2\theta\frac{\partial^2\delta\gamma}{\partial\phi^2} = 0, \tag{51}$$

where the last term in Eq. (50) arises from the Gaussian curvature of the spherical surface.

A general solution of Eqs. (50) and (51) for the perturbation Stokes flow is straightforward via separation of variables. In particular, the perturbation to the dynamic cap angle may be generally expanded as a sum of Fourier modes,

$$\delta\alpha(\phi,t)=\delta\alpha_n(t)e^{in\phi},\quad n=\pm2,\pm3,\ldots, \tag{52}$$

where the dilatational ($n=0$) and translational ($n=\pm1$) modes are omitted. In Appendix C, it is shown that the associated Fourier components of $\delta\psi$ and $\delta\gamma$ are given by

$$\begin{aligned}\frac{\delta\psi(\theta,\phi,t)}{i\epsilon R_0^2}&=\left\{a_n\cot^n\left(\frac{1}{2}\theta\right)+b_n\tan^n\left(\frac{1}{2}\theta\right)-c_n\sin^2\left(\frac{1}{2}\theta\right)\cot^n\left(\frac{1}{2}\theta\right)\right.\\&\left.-d_n\sin^2\left(\frac{1}{2}\theta\right)\tan^n\left(\frac{1}{2}\theta\right)\right\}\delta\alpha_n(t)e^{in\phi},\end{aligned} \tag{53}$$

$$\frac{\delta\gamma(\theta,\phi,t)}{\epsilon\eta_s R_0}=\frac{1}{2}\left\{\left[a_n+\frac{1}{2}(n-1)c_n\right]\cot^n\left(\frac{1}{2}\theta\right)-\left[b_n-\frac{1}{2}(n+1)d_n\right]\tan^n\left(\frac{1}{2}\theta\right)\right\}\delta\alpha_n(t)e^{in\phi}, \tag{54}$$

whose coefficients a_n, b_n, c_n, and d_n must now be determined from the boundary conditions at $\theta=0$ and $\alpha(t)$.

Applying boundedness conditions at the centerline gives

$$a_n=c_n=0 \tag{55}$$

for all $n=\pm2,\pm3,\ldots$. The remaining coefficients b_n and d_n are determined by applying the surface-stress condition at the edge of the domain [Eq. (7)]. Up to linear order in the perturbation variables, the normal and shear components of the stress condition simplify to

$$\left.\begin{aligned}\delta\sigma_{\theta\theta}&=-\frac{d\sigma_{\theta\theta}}{d\theta}\delta\alpha+\frac{\lambda}{R_0\sin^2\alpha}\left(\delta\alpha\cos^2\alpha+\frac{\partial^2\delta\alpha}{\partial\phi^2}\right)\\\delta\sigma_{\theta\phi}&=\frac{\sigma_{\phi\phi}-\sigma_{\theta\theta}}{\sin\alpha}\frac{\partial\delta\alpha}{\partial\phi}\end{aligned}\right\}\quad\text{at}\quad\theta=\alpha(t), \tag{56}$$

where the line tension λ has been retained. The base stresses $\sigma_{\theta\theta}$ and $\sigma_{\phi\phi}$ are derived from Eqs. (5), (40), and (41) as

$$\begin{aligned}\sigma_{\theta\theta}&=\gamma+\frac{\eta_s}{R_0}\left(\frac{dv_\theta}{d\theta}-v_\theta\cot\theta\right)\\&=\gamma_0+4\epsilon\eta_s\left\{\ln\left(\frac{1+\cos\theta}{1+\cos\alpha}\right)-\frac{1}{2}\left[\tan^2\left(\frac{1}{2}\alpha\right)-\tan^2\left(\frac{1}{2}\theta\right)\right]\right\},\end{aligned} \tag{57}$$

$$\begin{aligned}\sigma_{\phi\phi}&=\gamma-\frac{\eta_s}{R_0}\left(\frac{dv_\theta}{d\theta}-v_\theta\cot\theta\right)\\&=\gamma_0+4\epsilon\eta_s\left\{\ln\left(\frac{1+\cos\theta}{1+\cos\alpha}\right)-\frac{1}{2}\left[\tan^2\left(\frac{1}{2}\alpha\right)+\tan^2\left(\frac{1}{2}\theta\right)\right]\right\},\end{aligned} \tag{58}$$

while the perturbation stresses $\delta\sigma_{\theta\theta}$ and $\delta\sigma_{\theta\phi}$ are related to $\delta\gamma$ and $\delta\psi$ via

$$\delta\sigma_{\theta\theta}=\delta\gamma-\frac{2\eta_s\csc\theta}{R_0^2}\left(\frac{\partial^2\delta\psi}{\partial\theta\partial\phi}-\cot\theta\frac{\partial\delta\psi}{\partial\phi}\right), \tag{59}$$

$$\delta\sigma_{\theta\theta}=\frac{\eta_s}{R_0^2}\left(\frac{\partial^2\delta\psi}{\partial\theta^2}-\cot\theta\frac{\partial\delta\psi}{\partial\theta}-\csc^2\theta\frac{\partial^2\delta\psi}{\partial\phi^2}\right). \tag{60}$$

After inserting Eqs. (57)–(60) and (52)–(54) into (56), it is only a matter of algebra to derive the following expressions for the remaining Fourier coefficients:

$$b_n = \left[\frac{16\sin^4\left(\frac{1}{2}\alpha\right)}{\sin^3\alpha} - \frac{1}{\mathrm{Ca}}\left(\frac{n^2-\cos^2\alpha}{(n-1)\sin^2\alpha}\right)\right]\sin^2\left(\frac{1}{2}\alpha\right)\cot^n\left(\frac{1}{2}\alpha\right), \tag{61}$$

$$d_n = \left[\frac{16\sin^4\left(\frac{1}{2}\alpha\right)}{\sin^3\alpha} - \frac{1}{\mathrm{Ca}}\left(\frac{(n-\cos\alpha)(n^2-\cos^2\alpha)}{(n^2-1)\sin^2\alpha}\right)\right]\cot^n\left(\frac{1}{2}\alpha\right), \tag{62}$$

which depend upon the surface capillary number Ca [defined by Eq. (38)]. This completes the specification of the perturbation flow field.

Finally, to determine whether the shape perturbation will grow or decay in time, we expand the kinematic condition [Eq. (8)] up to linear order in the perturbation variables:

$$\frac{\partial\delta\alpha}{\partial t} = \frac{1}{R_0}\frac{dv_\theta}{d\theta}\delta\alpha + \frac{\delta v_\theta}{R_0} \quad \text{at} \quad \theta = \alpha(t). \tag{63}$$

Inserting Eqs. (40), (49), and (53) into (63) and invoking (55), (61), and (62) yields the evolution equation for the nth Fourier mode,

$$\frac{d\delta\alpha_n}{dt} \equiv \delta\dot{\alpha}_n = \epsilon s_n \delta\alpha_n, \tag{64}$$

where

$$s_n = \sec^2\left(\frac{1}{2}\alpha\right) - \frac{n}{2\mathrm{Ca}}\left(\frac{n^2-\cos^2\alpha}{(n^2-1)\sin\alpha}\right) \tag{65}$$

is the dimensionless growth rate. Since $\epsilon > 0$ under compression, Eq. (64) admits exponential growth of the modal perturbation $\delta\alpha_n(t)$ when $s_n > 0$. The first term on the right-hand side of Eq. (65) is always positive (destabilizing) and independent of the mode number. The second term is associated with line tension and is always negative (stabilizing), restoring circular shape symmetry. Therefore, the nth modal perturbation is expected to grow above a critical capillary number,

$$\mathrm{Ca} > \mathrm{Ca}_n \equiv \frac{n}{4}\left(\frac{n^2-\cos^2\alpha}{n^2-1}\right)\cot\left(\frac{1}{2}\alpha\right), \tag{66}$$

which is solely a function of the cap angle α. Equation (66) indicates that the critical condition for all modes diverges like $\mathrm{Ca}_n \sim n/(2\alpha)$ as $\alpha \to 0$, that is, small domains are stable against nonaxisymmetric perturbations. The most dangerous mode, $n = 2$, is the elliptic distortion. Figure 5 plots the ratio $\mathrm{Ca}_n/\mathrm{Ca}_2$ against α for various mode numbers, indicating that higher modes become unstable at successively larger compression rates.

The mechanism of the instability can be understood by examining only the crucial coupling term in the kinematic condition, Eq. (63):

$$\frac{\partial\delta\alpha}{\partial t} \approx \frac{1}{R_0}\frac{dv_\theta}{d\theta}\delta\alpha \quad \text{at} \quad \theta = \alpha(t), \tag{67}$$

which neglects the stabilizing term. Substituting the axisymmetric base flow from Eq. (40) into (67) yields the growth rate $(1/R_0)(dv_\theta/d\theta) = \epsilon\sec^2(\frac{1}{2}\alpha)$, corresponding to the first term on the right-hand side of Eq. (65). Thus, the instability is driven by the azimuthal perturbation $\delta\alpha$ coupling to the base velocity gradient $dv_\theta/d\theta$, which is positive under compression. A sketch of this mechanism is depicted in Fig. 6. This argument also explains why expansion of an axisymmetric cap is unconditionally stable to nonaxisymmetric perturbations: under expansion, the base flow v_θ reverses sign and so the velocity decays along the colatitude of the spherical cap. In this case, all modal perturbations decay with time rather than grow.

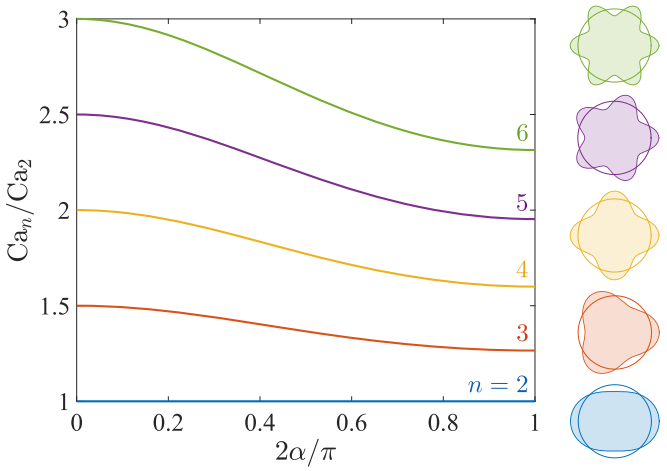

FIG. 5. Plots of the critical capillary number Ca_n of the nth Fourier mode (relative to that of the most dangerous mode, Ca_2) against the unperturbed cap angle α for various mode numbers $n = 2, 3, \ldots, 6$.

A useful point of contrast to the instability presented here is the famous Saffman-Taylor fingering instability of an inviscid fluid penetrating a viscous medium [52–56]. In the radial version of this instability [54], a circularly symmetric base flow decays radially outward from a point source injecting fluid at a constant volumetric flow rate. The velocity gradient associated with this base flow, therefore, has the opposite stability characteristics compared to the analogous $dv_\theta/d\theta$ term in the kinematic condition [see Eq. (63) or (67)]. This distinction can be clearly seen in Fig. 6, which depicts a radially accelerating flow of a surface-viscous domain penetrating a surface-inviscid phase. Thus, the mechanism of the Saffman-Taylor instability is entirely different. Its origin can be traced to the radial pressure gradient associated with the base flow, whose analog is the $-d\sigma_{\theta\theta}/d\theta$ term in the stress condition [Eq. (56)]. This radial pressure gradient couples to an angular, wavelike perturbation of the fluid front to induce a perturbation flow that further amplifies the waves. Surface tension (i.e., the Laplace pressure) acts in opposition to this pressure gradient to maintain circular symmetry. By contrast, the perturbation velocity δv_θ that appears in Eq. (63) is solely driven by the line tension λ and, therefore, is purely stabilizing.

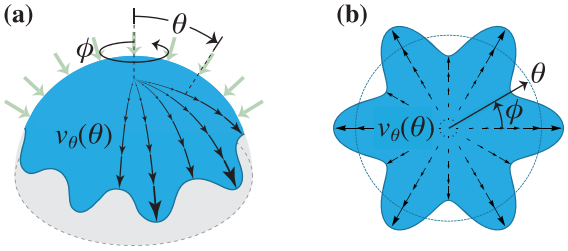

FIG. 6. Mechanism of nonaxisymmetric domain shape instability. (a) Compression of a surface-incompressible, spherical cap induces an axisymmetric base flow $v_\theta(\theta)$ that increases in speed along the colatitude θ. Consequently, a sinusoidal shape perturbation along the azimuth ϕ amplifies at the crests at a faster rate compared to the troughs. (b) Planar projection of the shape instability.

IV. DISCUSSION

In this paper, we have analyzed the dynamics of a surface-viscous domain of characteristic size $R_0\alpha_0$ on a spherical surface subject to a time-varying pressure perturbation. Our objective was to elucidate the processes by which surface-viscous stresses resist curvature deformation and break domain shape symmetry in curved, heterogeneous surface films, such as those found in surfactant-coated bubbles. From our theory, we identified two important time scales. The first timescale $\tau_D \equiv (R_0\alpha_0)^2/D = 4\eta_s\alpha_0^2/\gamma_0$ [Eq. (12)] characterizes the rate at which stress and curvature can relax diffusively across across a surface-viscous domain, and reflects the competition between surface-viscous stresses and surface tension. The second timescale $\tau_V \equiv R_0\alpha_0/V = \eta_s R_0\alpha_0/\lambda$ [Eq. (14)] weighs surface-viscous stresses against line tension and relates to the critical deformation rate at which the domain perimeter is unstable to small perturbations. Rendering each timescale dimensionless by either of the two rate scales, ω or ϵ, gives the dimensionless groups $\omega\tau_D = \mathrm{Pe}\,\alpha_0^2$ and $\epsilon\tau_V = \mathrm{Ca}\,\alpha_0$, which depend, respectively, on the Peclet number [Eq. (16)] and surface capillary number [Eq. (38)]. The quadratic and linear scalings with the static cap angle α_0 reflect the dependence on the domain surface area and perimeter, respectively, in the two relaxation processes.

Significantly, these predictions allow us to make some order-of-magnitude estimates for the curvature and shape dynamics of surface-viscous domains in surfactant monolayers. We can take dipalmitoylphosphatidylcholine (DPPC) in condensed-expanded phase coexistence as a prototypical system, since DPPC is the primary lipid component in lung surfactant [2,3] and ultrasound contrast agents [4,10]. Various viscometric measurements of DPPC report surface shear viscosities as large as $\eta_s \approx 100\ \mu\mathrm{N(s/m)}$ in a fully condensed monolayer (about 400 000 times the viscosity of a water layer of comparable thickness), which we take to be a reasonable value for the domain phase. The surface tension of DPPC in the coexistence region is consistently around $\gamma_0 \approx 60$ mN/m. By contrast, measurements of the line tension can vary [57–62] but are usually around $\lambda \approx 1$ pN. Domain-size distributions in the coexistence region are usually quite polydisperse [63,64], but for the sake of concreteness we will assume a typical size on the order of $R_0\alpha_0 \approx 5\ \mu$m. Finally, we take $R_0 \approx 40\ \mu$m as a characteristic radius of curvature for lung alveoli and ultrasound contrast agents.

Using these numbers, we estimate $\tau_D \approx 0.1$ ms as the characteristic timescale for the surface tension and curvature to relax by diffusion. This is a rapid relaxation process and reflects the dominance of the Laplace pressure (i.e., the static surface tension) over the surface shear viscosity in curved surface films—a comparison that is entirely masked in planar surfaces! In ultrasound contrast applications, acoustic driving frequencies around 1 MHz would easily outpace this relaxation process (i.e., the Peclet number $\mathrm{Pe} \gg \mathrm{Pe}^*$), producing highly anisotropic, oscillating bubbles with inhomogeneous surface curvature similar to observations by Dollet and coworkers [9]. By comparison, the timescale for domain shape relaxation is quite slow, $\tau_V \approx 0.5$ ks, due to the small line tension λ between the chemically similar (but structurally distinct) surface phases of DPPC. Noncircular domain shapes could, therefore, be realized with modest driving frequencies; e.g., 1 Hz is a typical breathing frequency for human lungs [corresponding to a capillary number $\mathrm{Ca} \gg \mathrm{Ca}_n$ up to $n = O(1000)$]. This outcome further justifies our original insight to focus on only the slowest frequencies when analyzing the linear stability of circular domain shapes.

In addition to making quantitative predictions of relaxation processes in curved surface films, our theory also provides useful insight into the micro-scale physics underlying these processes. For instance, our analysis of axisymmetric curvature deformations of a surface-viscous domain revealed the large increase in stress across a thin boundary layer near the domain border when oscillated at high frequency [Fig. 3 and Eqs. (32)–(34)]. Moreover, we found that the amplitude of these deformations is maximized at an intermediate Peclet number $\approx 3\,\mathrm{Pe}^*$ that is solely a function of the equilibrium cap angle α_0 [Fig. 4 and Eq. (36)]. When analyzing nonaxisymmetric perturbations to the domain shape, we revealed a linear instability whereby the surface

flow induced by compressing the domain surface (i.e., increasing its curvature) amplifies the perturbations (Fig. 6). The opposite (stabilizing) effect occurs when the surface is expanded rather than compressed. Important distinctions from the classical Saffman-Taylor instability—that is, the fingering of an inviscid fluid being injected into a viscous medium—were discussed at the end of Sec. III B.

Although the results presented in this paper were entirely theoretical, various experimental avenues exist for testing our predictions. The state-of-the-art apparatus for measuring the dynamic surface behavior of DPPC and other surfactants on spherical fluid interfaces of diameters less than 1 mm is the microbubble tensiometer [65–75]. In this measurement technique, a bubble surface coated with surfactant is oscillated by sinusoidally modulating the capillary pressure (typical frequencies less than 1 Hz) while simultaneously monitoring the surface shape via optical microscopy. If the condensed (domain) and expanded (continuum) phases of the surfactant are optically distinguishable (e.g., by binding a fluorescent tag to a trace component that preferentially segregates to the expanded phase), then such a technique could be used to investigate the stability of surface domains by confocal sectioning of the bubble surface. The key prediction to test is the instability criterion $\mathrm{Ca} > \mathrm{Ca}_n$ [see Eq. (66)], which requires at a minimum estimates for the line tension λ and surface shear viscosity η_s of the domains. This strategy is limited, of course, by the scanning rate of the confocal microscope as well as the challenges associated with optically tracking a moving interface with varying curvature.

As the microbubble tensiometer is practically limited to slow frequencies (less than 1 Hz), it is inadequate for studying the high-frequency dynamics that generate anisotropic bubble curvatures. Ultrasound driving frequencies ($\sim$1 MHz) are better suited to this task, supplemented by a method to visualize the domain surface microstructure under static conditions. Here, the criterion (to be tested) for nonspherical surface oscillations is $\mathrm{Pe} \gg \mathrm{Pe}^*$ [see Eq. (36)], which depends upon the static surface tension γ_0 and surface shear viscosity η_s of the domain phase. Additionally, a frequency sweep of the shape response could reveal interesting non-monotonic behavior such as that reported in Fig. 4. Similar techniques have been used to analyze inertially driven, nonspherical bubble oscillations [9].

Of course, any attempts at validating or verifying the predictions presented in this paper must also take into account the limitations of (and assumptions behind) the present theory. First, there are several physical processes that are neglected in our theory that nevertheless play an important role in real surfactant systems. One important example is the phase condensation or melting processes that can occur when a surfactant monolayer is compressed or expanded, respectively. Such processes are driven by a mismatch in chemical potential between the surface-viscous and surface-inviscid phases when forced out of equilibrium. Several authors [76] have examined the coupled processes of surface-incompressible fluid flow and phase transfer through Stefan- and Gibbs-Thomson-type boundary conditions, but these are beyond the scope of the present paper. In our theory, we have assumed that the surface-viscous domain maintains a constant surface area and, therefore, no such mass transfer occurs between it and the surface-inviscid phase. This assumption is almost certainly an oversimplification for typical driving frequencies, because the rate of phase transfer is usually quite fast. We do not expect phase transfer to significantly impact the curvature deformations predicted by our axisymmetric model, for the following reason: At high enough frequencies, surface-viscous stresses would eventually overwhelm any stresses generated by an imbalance in chemical potential, the latter of which are primarily dictated by the amplitude (less so the rate) of compression or expansion. However, we *do* expect that phase transfer could qualitatively impact the growth of angular, wavelike distortions of the domain perimeter, due to the inhomogeneous mass-transfer fluxes that are established at the crests and troughs of the waves. This diffusive mechanism is the basis for the Mullins-Sekerka fingering instabilities that have been previously reported for surfactant domains [77–82]. By neglecting phase transfer, we have implicitly assumed that the typical size $R_0\alpha_0$ of the domain considered in this paper is smaller than the critical nucleus size for diffusive fingering [83].

Besides phase transformation processes, our model also neglects the electrostatic dipole forces that are known to play a role in phase-coexisting surfactant systems [14,84–86]. These repulsive forces inhibit the coarsening and coalescence of condensed domains and destabilize circularly symmetric domain shapes. In their absence, line tension λ drives domains to coarsen (i.e., Ostwald ripen) and remain symmetric. Thus, a competition between a 2D Laplace pressure (due to λ) and an apparently negative, electrostatic pressure determines the equilibrium domain morphology in both planar [84,85,87] and curved [88] surfaces. In our theory, we have assumed a line-tension-dominant morphology whereby the static domain shape is circular and interactions with other domains in the surface are neglected. In this regime, we do not expect electrostatic forces to qualitatively impact the dynamics.

Other simplifications were invoked at the outset to focus only on the essential physics without convoluting the main results. Nevertheless, these simplifications limit the applicability of our model to a wider parameter space and, for that reason, merit some discussion. For one, the only dissipative process that was considered is attributed to the surface-viscous stresses within the domain itself. Bulk viscous stresses, which were mentioned briefly in the paragraphs following Eq. (6), could also contribute to momentum dissipation if the Boussinesq number Bq is of $O(1)$. Related to this is the presumption of a surface-inviscid exterior phase surrounding the domain, which was motivated by the large disparity in surface viscosities between fully condensed and expanded surfactant films [21]. In reality, accounting for the small (but finite) exterior surface viscosity could attenuate the relaxation dynamics predicted by our theory. However, this effect is expected to be more quantitative than qualitative.

A more consequential modification of the present model would include a finite dilatational viscosity κ_s of the surface domain phase, allowing it to compress or expand in addition to shear. In Eq. (4), surface-area incompressibility was implicitly assumed provided that the dilatational timescale,

$$\tau_K \equiv \frac{4\kappa_s \alpha_0^2}{\gamma_0}, \tag{68}$$

is sufficiently large. This is generally a good assumption for condensed phases of surface-adsorbed, insoluble surfactants (e.g., DPPC), which are shearable but only weakly compressible in the monolayer surface. When this condition is not met, however, then the incompressibility equation [Eq. (4)] has to be replaced by a mass-conservation equation governing the evolution of the surface mass density $\rho_s(\theta, \phi, t)$,

$$\frac{\partial \rho_s}{\partial t} + \boldsymbol{\nabla}_s \cdot (\rho_s \boldsymbol{v}_s) + \frac{2\rho_s}{R_0}\frac{\partial R}{\partial t} = 0, \tag{69}$$

and the Boussinesq-Scriven constitutive law [Eq. (5)] must be modified to include the dilatational stresses,

$$\boldsymbol{\sigma}_s = \gamma \boldsymbol{\delta}_s + \eta_s[(\boldsymbol{\nabla}_s \boldsymbol{v}_s) \cdot \boldsymbol{\delta}_s + \boldsymbol{\delta}_s \cdot (\boldsymbol{\nabla}_s \boldsymbol{v}_s)^\top - (\boldsymbol{\nabla}_s \cdot \boldsymbol{v}_s)\boldsymbol{\delta}_s] + \kappa_s \left(\boldsymbol{\nabla}_s \cdot \boldsymbol{v}_s + \frac{2}{R_0}\frac{\partial R}{\partial t} \right) \boldsymbol{\delta}_s, \tag{70}$$

along with a suitable equation of state relating ρ_s to the (thermodynamic) surface tension γ. Using Eqs. (69) and (70), the tangential momentum equation [Eq. (6)] is modified to read

$$\boldsymbol{\delta}_s \cdot (\boldsymbol{\nabla}_s \cdot \boldsymbol{\sigma}_s) = \boldsymbol{\nabla}_s \gamma + \eta_s \boldsymbol{\delta}_s \cdot \left(\nabla_s^2 \boldsymbol{v}_s + \frac{2\boldsymbol{v}_s}{R_0^2} \right) - \kappa_s \boldsymbol{\nabla}_s \Delta = \boldsymbol{0}, \tag{71}$$

where

$$\Delta \equiv \frac{d \ln \rho_s}{dt} = \frac{1}{\rho_s}\left(\frac{\partial \rho_s}{\partial t} + \boldsymbol{v}_s \cdot \boldsymbol{\nabla}_s \rho_s \right) = -\boldsymbol{\nabla}_s \cdot \boldsymbol{v}_s - \frac{2}{R_0}\frac{\partial R}{\partial t} \tag{72}$$

is the rate of surface dilatation. Equations (69)–(71) simplify to (4)–(6) when $\rho_s =$ constant.

We have analyzed the general problem of surface-compressible, viscous domains with surface viscosities κ_s and η_s in the linear-response limit of a weak, sinusoidal pressure forcing, assuming that the thermodynamic tension is approximately equal to the static tension ($\gamma \approx \gamma_0$). Here, we will briefly summarize some key results (the details of our analysis can be found in Appendix D). We find that mass diffuses along the surface with a modified diffusion coefficient

$$D = \frac{\gamma_0 R_0^2}{\zeta_s}, \tag{73}$$

and an effective viscosity given by

$$\zeta_s = \frac{4\kappa_s \eta_s}{\kappa_s + \eta_s}. \tag{74}$$

The latter quantity is equivalent to the Young's viscosity of thin, continuum sheets. We also find that our predictions for the frequency-dependent relaxation of surface curvature and tension remain valid if we simply redefine the Peclet number as

$$\mathrm{Pe} \equiv \frac{\omega R_0^2}{D} = \frac{\omega \zeta_s}{\gamma_0}, \tag{75}$$

with the Young's viscosity ζ_s given by Eq. (74). Taking the incompressible limit as $\omega\kappa_s/\gamma_0 \to \infty$ while holding $\omega\eta_s/\gamma_0$ finite recovers our original definition of the Peclet number, $\mathrm{Pe} = 4\omega\eta_s/\gamma_0$ [see Eq. (16)]. In this regime, all our previous analyses of axisymmetric deformations can be applied directly without further modification. In the opposite limit as $\omega\kappa_s/\gamma_0 \to 0$, where resistance to areal compression is negligible, $\mathrm{Pe} = 0$ and so the curvature of the domain relaxes as though it were a surface-inviscid, gaseous phase. In this respect, compliance to either surface dilatation ($\omega\kappa_s/\gamma_0 \ll 1$) or surface shear ($\omega\eta_s/\gamma_0 \ll 1$) effect similar dynamics: in both regimes, the Peclet number $\mathrm{Pe} \ll 1$. This is intuitive if we interpret Eq. (74) as the effective resistance of an equivalent circuit with resistive elements κ_s and η_s arranged in parallel. Diffusion (i.e., the current) through the circuit always takes the path of least resistance, favoring either dilatation (κ_s) or shear (η_s) depending on which is the softer element. Only when both the shear and dilatational viscosities are large compared to γ_0/ω (i.e., $\mathrm{Pe} \gg 1$) will the curvature cease to relax on $O(\omega^{-1})$ timescales. In most condensed surfactant systems of interest, the surface shear viscosity η_s is expected to limit the high-frequency dynamics and, therefore, our simplified model of surface-incompressible domains is appropriate.

The related problem of analyzing the circular shape instability of surface-compressible domains with finite dilatational viscosity remains open to future investigation. Without performing a detailed calculation, it is straightforward to deduce that the surface flow produced by an increase in curvature will accelerate radially outward from the domain center, irrespective of its viscous properties. This leads us to surmise that the basic mechanism of instability will be similar to the one discussed previously (see Fig. 6), wherein a positive velocity gradient amplifies shape perturbations above a critical deformation rate. However, the exact instability criterion, including specification of the mode-dependent, critical capillary number Ca_n, requires more thorough analysis and is beyond the scope of the present study.

Finally, our model has focused entirely on surface-viscous domains, neglecting the elastic (or viscoelastic) behavior that is frequently observed in a variety of surfactant systems (e.g., those that form cohesive networks and surface gels [89,90]). Extending this model to linearly viscoelastic domains is trivial via Pipkin's correspondence principle [91]. For instance, the purely viscous moduli $i\omega\eta_s$ and $i\omega\kappa_s$ that characterize the linear frequency dynamics can be replaced, respectively, by the complex surface shear modulus G_s^* and dilatational modulus E_s^*. The real (elastic) and imaginary (viscous) parts of these moduli reflect, respectively, the ability of the surface domain to store or dissipate energy under either shear or compression. Ultimately, the amplitude of the surface Young's modulus $Y_s^* = 4E_s^* G_s^*/(E_s^* + G_s^*)$ [the linear-viscoelastic analog of $i\omega\zeta_s$ from Eq. (74)] determines the frequency dependence of the linear response, with the Peclet number [Eq. (75)]

redefined appropriately in terms of $|Y_s^*|$. In mimicking heterogeneous, viscoelastic surfactants, a more faithful model might also have to account for the surface moduli of the exterior, embedding phase (in addition to those of the domain phase). This, in turn, would add four more material functions (the real and imaginary parts of the shear and dilatational moduli) that must be specified in the model.

Less trivial (and more interesting) differences between viscous and viscoelastic materials emerge if we look beyond the linear-response limit to *nonlinear* curvature deformations. Nonlinear effects were briefly discussed at the end of Sec. III A in the context of wrinkling and buckling instabilities that can emerge in viscous sheets deformed at a rapid rate. In elastic materials, stresses due to geometric nonlinearities emerge when the material is strained by an appreciable degree from its stress-free or reference state, regardless of the rate of straining. (Small strains are still required for *material* nonlinearities to be safely neglected.) Such nonlinearities are generally unimportant for surface-viscous materials, whose stresses admit a linear dependence on the velocity gradients [see Eq. (5)]. By contrast, the stresses in surface-elastic materials are history dependent and can depend nonlinearly on the displacement gradients for large enough departures from the reference surface. Our model implicitly assumes a reference spherical surface of radius R_0 under a static pressure p_0, so Eq. (3) accurately captures the incremental displacement δR that results from a small pressure perturbation δp. In this linearized regime, the differential operators in the mass and momentum conservation equations [Eqs. (4)–(6) and their linear-viscoelastic analogs] are evaluated on the reference sphere. For large enough pressure perturbations, deviations from this reference surface become significant and, in the case of elastic materials, nonlinear strains cannot be neglected in the constitutive model.

V. CONCLUSIONS

In summary, our model of a two-phase surface undergoing a time-varying curvature deformation reveals several interesting phenomena that are absent in planar or homogeneous interfaces. Domains with large surface shear viscosity resist changes in curvature compared to a surface-inviscid phase. Consequently, the curvature of a two-phase surface can become heterogeneous upon sufficiently rapid deformation. We showed that the curvature of surface-viscous domains relaxes diffusively on a timescale set by the surface tension (or Laplace pressure). Additionally, large domains are prone to a symmetry-breaking shape instability under (relatively slow) compression. The growth of such instabilities is retarded by line tension.

Future work could generalize our model to more exotic two-phase and multiphase morphologies, as well as nonspherical curved geometries. In such generalizations, the key physical ingredient of our model to be preserved is the varying Gaussian curvature, which (through surface-incompressibility) induces the 2D Stokes flows that produce interesting and nontrivial dynamics. Our study focused on spherical surfaces (with positive Gaussian curvature), but various nonspherical surfaces including conical threads and hyperboloids (with negative Gaussian curvature) have clear engineering applications. Finally, constitutive models with history-dependent surface rheology, including elasticity and viscoelasticity, could qualitatively impact the dynamics of our model and merit future investigation.

ACKNOWLEDGMENTS

The research reported in this publication was supported by the National Heart, Lung, and Blood Institute of the National Institutes of Health (Grants No. R01HL135065 and No. R01HL051177). J.M.B. was supported by the NIH F32 Ruth L. Kirschstein National Research Service Award (Grant No. F32HL156366). The content is solely the responsibility of the authors and does not necessarily represent the official views of the National Institutes of Health.

APPENDIX A: DERIVATION OF THE SURFACE DIFFUSION EQUATIONS

Equations (9) and (10) may be derived from Eqs. (3), (4), and (6) as follows. Taking the surface divergence of the tangential momentum equation [Eq. (6)] gives

$$\nabla_s^2\gamma + \eta_s\left(\nabla_s^2(\boldsymbol{\nabla}_s\cdot\boldsymbol{v}_s) + \frac{2}{R_0^2}(\boldsymbol{\nabla}_s\cdot\boldsymbol{v}_s)\right) = 0. \tag{A1}$$

Then, the incompressibility equation [Eq. (4)] is used to eliminate the surface dilatation rate $(\boldsymbol{\nabla}_s\cdot\boldsymbol{v}_s)$ from Eq. (A1):

$$\nabla_s^2\gamma - \frac{2\eta_s}{R_0}\frac{\partial}{\partial t}\left(\nabla_s^2 R + \frac{2R}{R_0^2}\right) = 0. \tag{A2}$$

Equation (A2) is a second relationship between the surface tension γ and the surface curvature perturbation $\nabla_s^2 R + 2R/R_0^2$, the first being the normal momentum equation [Eq. (3)]. Eliminating $\nabla_s^2 R + 2R/R_0^2$ between Eqs. (3) and (A2) results in Eq. (9), whereas eliminating γ gives Eq. (10).

APPENDIX B: SINGULAR PERTURBATION ANALYSIS FOR LARGE PECLET NUMBER

Equations (32)–(34) may be derived by matched asymptotic expansions, assuming a boundary layer of $O(\mathrm{Pe}^{-\frac{1}{2}})$ thickness near the edge of the spherical cap [at $\theta = \alpha_0$]. In the outer region far from the boundary layer, the $O(\mathrm{Pe}^{-1})$ term in Eq. (23) may be neglected to leading order. The velocity field is then determined by solving a homogeneous equation with symmetry at the centerline,

$$\delta\bar{v}_\theta^{\,o} = [a_0 + (i\mathrm{Pe})^{-\frac{1}{2}}a_1]\sin\theta + O(\mathrm{Pe}^{-1}), \tag{B1}$$

where the superscript "o" denotes the outer solution and the constants a_0, a_1 associated with the first two terms in the expansion must be determined by matching to the corresponding inner solution. Substituting Eq. (B1) into (22) then yields the outer expansion for the cap radius,

$$\delta\bar{R}^{o} = -[a_0 + (i\mathrm{Pe})^{-\frac{1}{2}}a_1]\cos\theta + O(\mathrm{Pe}^{-1}), \tag{B2}$$

and subsequently inserting Eq. (B2) into (21) gives the particular solution for the surface tension:

$$\delta\bar{\gamma}^{\,o} = \delta\bar{p} + O(\mathrm{Pe}^{-1}). \tag{B3}$$

The outer expansions fail to satisfy the boundary conditions at $\theta = \alpha_0$. This problem may be rectified by stretching the independent variable,

$$\Theta = (i\mathrm{Pe})^{\frac{1}{2}}(\alpha_0 - \theta), \tag{B4}$$

and solving a boundary-layer problem over the inner region $0 \leqslant \Theta < \infty$. In this region, the tension grows exponentially in order to compensate for the rapid change in curvature across the boundary layer. This exponential growth is most easily seen by rescaling the surface tension as

$$\delta\bar{\Gamma} = (i\mathrm{Pe})^{-\frac{1}{2}}\delta\bar{\gamma} \tag{B5}$$

and rescaling the surface diffusion equation [Eq. (9)] for the inner region:

$$\frac{d^2\delta\bar{\Gamma}}{d\Theta^2} - \delta\bar{\Gamma} + (i\mathrm{Pe})^{-\frac{1}{2}}\left(\delta\bar{p} - \cot\alpha_0\frac{d\delta\bar{\Gamma}}{d\Theta}\right) = O(\mathrm{Pe}^{-1}). \tag{B6}$$

[This expression replaces Eq. (4) to enforce local surface incompressibility.] The solution up to $O(\mathrm{Pe}^{-1})$ is

$$\delta\bar{\Gamma}^{i} = b_0 e^{-\Theta} + (i\mathrm{Pe})^{-\frac{1}{2}}\left\{\delta\bar{p} + \left[b_1 + \tfrac{1}{4}b_0(\cot\alpha_0)(1+2\Theta)\right]e^{-\Theta}\right\} + O(\mathrm{Pe}^{-1}), \tag{B7}$$

where the superscript "i" denotes the inner solution and b_0, b_1 are two new constants of integration. Equation (B7) clearly reveals the exponential variation in surface tension across the boundary layer and may be used to determine the inner expansions for $\delta\bar{R}$ and $\delta\bar{v}_\theta$. The latter obey the stretched momentum balance equations [see Eqs. (21) and (23)],

$$\frac{d^2\delta\bar{R}}{d\Theta^2} - (i\mathrm{Pe})^{-\frac{1}{2}}\left(\delta\bar{\Gamma} + \cot\alpha_0\frac{d\delta\bar{R}}{d\Theta}\right) = O(\mathrm{Pe}^{-1}), \tag{B8}$$

$$\frac{d^2\delta\bar{v}_\theta}{d\Theta^2} - (i\mathrm{Pe})^{-\frac{1}{2}}\cot\alpha_0\frac{d\delta\bar{v}_\theta}{d\Theta} = O(\mathrm{Pe}^{-1}), \tag{B9}$$

subject to the surface stress boundary conditions at $\Theta = 0$ [see Eq. (25)]:

$$\frac{d\delta\bar{R}}{d\Theta} = 0, \quad \frac{d\delta\bar{v}_\theta}{d\Theta} + (i\mathrm{Pe})^{-\frac{1}{2}}\delta\bar{v}_\theta\cot\alpha_0 = O(\mathrm{Pe}^{-1}). \tag{B10}$$

Substituting Eq. (B7) into (B8) for $\delta\bar{\Gamma}$ and sequentially integrating Eqs. (B8) and (B9) with the boundary conditions Eqs. (B10) then gives the inner expansions,

$$\delta\bar{R}^{\mathrm{i}} = c_0 + (i\mathrm{Pe})^{-\frac{1}{2}}[c_1 + 2b_0(\Theta + e^{-\Theta})] + O(\mathrm{Pe}^{-1}), \tag{B11}$$

$$\delta\bar{v}_\theta^{\mathrm{i}} = -c_0\tan\alpha_0 - (i\mathrm{Pe})^{-\frac{1}{2}}(c_1\tan\alpha_0 - c_0\Theta) + O(\mathrm{Pe}^{-1}), \tag{B12}$$

with two new integration constants c_0, c_1 to be determined from matching to the outer solution. Applying an integral force balance on the cap [see Eq. (28)] gives the final boundary condition,

$$\delta\bar{R}^{\mathrm{i}} = -\delta\bar{p} \quad \text{at} \quad \Theta = 0, \tag{B13}$$

which ensures that the surface is continuous across the interphase boundary. Using Eqs. (B11) and (B13), this leads to the additional constraints:

$$c_0 = -\delta\bar{p}, \quad c_1 = -2b_0. \tag{B14}$$

Matching between the outer and inner solutions may be performed using van Dyke's matching rule [92]. First, we express the outer in terms of inner expansions by Taylor-expanding Eqs. (B1)-(B3) about $\theta = \alpha_0$ and rewriting the expansions in terms of the inner variable [Eq. (B4)]:

$$\left(\delta\bar{v}_\theta^{\mathrm{o}}\right)^{\mathrm{i}} = a_0\sin\alpha_0 + (i\mathrm{Pe})^{-\frac{1}{2}}[a_1\sin\alpha_0 - (a_0\cos\alpha_0)\Theta] + O(\mathrm{Pe}^{-1}), \tag{B15}$$

$$(\delta\bar{\gamma}^{\mathrm{o}})^{\mathrm{i}} = \delta\bar{p} + O(\mathrm{Pe}^{-1}), \tag{B16}$$

$$(\delta\bar{R}^{\mathrm{o}})^{\mathrm{i}} = -a_0\cos\alpha_0 - (i\mathrm{Pe})^{-\frac{1}{2}}[a_1\cos\alpha_0 + (a_0\sin\alpha_0)\Theta] + O(\mathrm{Pe}^{-1}). \tag{B17}$$

Similarly, the inner in terms of outer expansions are obtained by evaluating Eqs. (B7), (B11), and (B12) in the limit as $\Theta \to \infty$, wherein the exponential terms die off:

$$\left(\delta\bar{v}_\theta^{\mathrm{i}}\right)^{\mathrm{o}} = -c_0\tan\alpha_0 - (i\mathrm{Pe})^{-\frac{1}{2}}(c_1\tan\alpha_0 - c_0\Theta) + O(\mathrm{Pe}^{-1}), \tag{B18}$$

$$(\delta\bar{\Gamma}^{\mathrm{i}})^{\mathrm{o}} = (i\mathrm{Pe})^{-\frac{1}{2}}\delta\bar{p} + O(\mathrm{Pe}^{-1}), \tag{B19}$$

$$(\delta\bar{R}^{\mathrm{i}})^{\mathrm{o}} = c_0 + (i\mathrm{Pe})^{-\frac{1}{2}}(c_1 + 2b_0\Theta) + O(\mathrm{Pe}^{-1}). \tag{B20}$$

Applying the matching conditions,

$$\left(\delta\bar{v}_\theta^{\mathrm{o}}\right)^{\mathrm{i}} = (\delta\bar{v}_\theta^{\mathrm{i}})^{\mathrm{o}}, \tag{B21}$$

$$(\delta\bar{\gamma}^{\mathrm{o}})^{\mathrm{i}} = (i\mathrm{Pe})^{\frac{1}{2}}(\delta\bar{\Gamma}^{\mathrm{i}})^{\mathrm{o}}, \tag{B22}$$

$$(\delta\bar{R}^{\mathrm{o}})^{\mathrm{i}} = (\delta\bar{R}^{\mathrm{i}})^{\mathrm{o}}, \tag{B23}$$

and equating terms of like order in Θ and $\mathrm{Pe}^{-\frac{1}{2}}$ leads to the set of simultaneous equations,

$$a_0\cos\alpha_0 = -c_0, \quad a_1\cos\alpha_0 = -c_1, \quad a_0\sin\alpha_0 = -2b_0. \tag{B24}$$

Solving Eqs. (B14) and (B24) then gives

$$\left.\begin{aligned} a_0 = \frac{\delta\bar{p}}{\cos\alpha_0}, \quad a_1 = \frac{\delta\bar{p}\tan\alpha_0}{\cos\alpha_0}, \quad b_0 = -\frac{1}{2}\delta\bar{p}\tan\alpha_0, \\ c_0 = -\delta\bar{p}, \quad c_1 = \delta\bar{p}\tan\alpha_0, \end{aligned}\right\}, \tag{B25}$$

with only the constant b_1 [appearing in Eq. (B7)] left undetermined at this order. It is then straightforward to show that insertion of Eqs. (B1)–(B3), (B7), (B11)–(B12), (B15)–(B17), and (B25) into the composite expansions,

$$\delta\bar{v}_\theta = \delta\bar{v}_\theta^{\,\mathrm{o}} + \delta\bar{v}_\theta^{\,\mathrm{i}} - \left(\delta\bar{v}_\theta^{\,\mathrm{o}}\right)^{\mathrm{i}}, \tag{B26}$$

$$\delta\bar{\gamma} = \delta\bar{\gamma}^{\mathrm{o}} + (i\mathrm{Pe})^{\frac{1}{2}}\delta\bar{\Gamma}^{\mathrm{i}} - (\delta\bar{\gamma}^{\mathrm{o}})^{\mathrm{i}}, \tag{B27}$$

$$\delta\bar{R} = \delta\bar{R}^{\mathrm{o}} + \delta\bar{R}^{\mathrm{i}} - (\delta\bar{R}^{\mathrm{o}})^{\mathrm{i}}, \tag{B28}$$

leads directly to Eqs. (32)–(34) in the main text.

APPENDIX C: GENERAL SOLUTION FOR THE PERTURBATION FLOW ON A SPHERE

In this Appendix, we derive a general solution of Eqs. (50) and (51) that is forced by an n-fold harmonic distortion of the domain perimeter [Eq. (52)]. First, by linearity of the surface Stokes equations, we may express $\delta\psi$ and $\delta\gamma$ in the separated form

$$\delta\psi(\theta,\phi,t) = \delta\psi_n(\theta)\delta\alpha_n(t)e^{in\phi}, \tag{C1}$$

$$\delta\gamma(\theta,\phi,t) = \delta\gamma_n(\theta)\delta\alpha_n(t)e^{in\phi}, \tag{C2}$$

with $n = \pm 2, \pm 3, \ldots$. Then, substituting Eqs. (C1)–(C2) into (50) and (51) yields a set of ordinary differential equations for the amplitude functions $\delta\psi_n(\theta)$ and $\delta\gamma_n(\theta)$:

$$\mathcal{L}_{0|n}\mathcal{L}_{1|n}\delta\psi_n = 0, \tag{C3}$$

$$\mathcal{L}_{0|n}\delta\gamma_n = 0, \tag{C4}$$

where we have defined the associated Legendre operator,

$$\mathcal{L}_{l|n} \equiv \frac{d^2}{d\theta^2} + \cot\theta\frac{d}{d\theta} + l(l+1) - n^2\csc^2\theta. \tag{C5}$$

For the sake of simplicity, we shall focus on only the positive modes ($n \geqslant 2$), with the understanding that the negative modes for real-valued functions are obtained via complex conjugation. The eigenfunctions $f^+_{l|n}(\theta)$ and $f^-_{l|n}(\theta)$ associated with the operator defined by Eq. (C5) satisfy the homogeneous equation,

$$\mathcal{L}_{l|n}f^\pm_{l|n}(\theta) = 0, \tag{C6}$$

and, for $n > l$ (assuming n is positive), are given explicitly by Hobson [93]:

$$f^\pm_{l|n}(\theta) = (\pm 1)^n n\sin^n\theta\int_{\pm 1}^{\pm\infty}\frac{P_l(x)}{(x-\cos\theta)^{n+1}}\,dx. \tag{C7}$$

Of particular interest are the eigenfunctions of degrees $l = 0$,

$$f^+_{0|n}(\theta) = \cot^n\left(\tfrac{1}{2}\theta\right), \tag{C8}$$

$$f^-_{0|n}(\theta) = \tan^n\left(\tfrac{1}{2}\theta\right), \tag{C9}$$

and $l = 1$:

$$f^{+}_{1|n}(\theta) = \frac{(\cos\theta - n)\cot^n\left(\frac{1}{2}\theta\right)}{1-n}, \tag{C10}$$

$$f^{-}_{1|n}(\theta) = \frac{(\cos\theta + n)\tan^n\left(\frac{1}{2}\theta\right)}{1-n}. \tag{C11}$$

Clearly, $f^{+}_{0|n}(\theta)$ and $f^{-}_{0|n}(\theta)$ are eigenfunctions of Eqs. (C3) and(C4). Two additional eigenfunctions of Eq. (C3), denoted by $g^{+}_{1|n}(\theta)$ and $g^{-}_{1|n}(\theta)$, are obtained by the method of variation of parameters:

$$g^{\pm}_{1|n}(\theta) = \frac{1}{2n}\left(f^{-}_{0|n}(\theta)\int^{\theta} f^{+}_{0|n}(\theta')f^{\pm}_{1|n}(\theta')\sin\theta'\,d\theta' - f^{+}_{0|n}(\theta)\int^{\theta} f^{-}_{0|n}(\theta')f^{\pm}_{1|n}(\theta')\sin\theta'\,d\theta'\right). \tag{C12}$$

Inserting Eqs. (C8)–(C11) into (C12) and evaluating the indefinite integrals over θ' gives

$$g^{+}_{1|n}(\theta) = \frac{\sin^2\left(\frac{1}{2}\theta\right)\cot^n\left(\frac{1}{2}\theta\right)}{1-n}, \tag{C13}$$

$$g^{-}_{1|n}(\theta) = \frac{\sin^2\left(\frac{1}{2}\theta\right)\tan^n\left(\frac{1}{2}\theta\right)}{1-n}. \tag{C14}$$

In summary, a general solution for $\delta\psi_n$ is obtained from a linear combination of $f^{+}_{0|n}$, $f^{-}_{0|n}$, $g^{+}_{1|n}$ and $g^{-}_{1|n}$:

$$\frac{\delta\psi_n(\theta)}{i\epsilon R_0^2} = \left[a_n - c_n\sin^2\left(\frac{1}{2}\theta\right)\right]\cot^n\left(\frac{1}{2}\theta\right) + \left[b_n - d_n\sin^2\left(\frac{1}{2}\theta\right)\right]\tan^n\left(\frac{1}{2}\theta\right), \tag{C15}$$

where we have deliberately factored out $i\epsilon R_0^2$ so the constants a_n, b_n, c_n, and d_n are dimensionless. Similarly, the general solution for $\delta\gamma_n$ is a linear combination of $f^{+}_{0|n}$ and $f^{-}_{0|n}$,

$$\frac{\delta\gamma_n(\theta)}{\epsilon\eta_s R_0} = e_n\cot^n\left(\frac{1}{2}\theta\right) - f_n\tan^n\left(\frac{1}{2}\theta\right), \tag{C16}$$

where $\epsilon\eta_s R_0$ has been factored and e_n and f_n are additional constants. The unknown constants a_n, b_n, c_n, d_n, e_n, and f_n are not linearly independent—they are coupled through the two independent components of the momentum conservation equation [Eq. (6)]. Indeed, this equation is only satisfied if

$$\left.\begin{aligned} e_n &= \tfrac{1}{2}\left[a_n + \tfrac{1}{2}(n-1)c_n\right] \\ f_n &= \tfrac{1}{2}\left[b_n - \tfrac{1}{2}(n+1)d_n\right] \end{aligned}\right\}. \tag{C17}$$

It is then straightforward to show that Eqs. (C1) and (C2) and (C15)–(C17) lead directly to Eqs. (53) and (54) in the main text.

APPENDIX D: EFFECT OF FINITE DILATATIONAL VISCOSITY

The results presented in Sec. III A were derived under the assumption of surface incompressibility. In this Appendix, we revisit this problem for a surface-compressible domain with a finite surface dilatational viscosity κ_s. The crucial difference comes from replacing the surface momentum and mass balance equations [Eqs. (4)–(6)] with their more general forms, Eqs. (69)–(71). This replacement introduces the surface mass density $\rho_s(\theta, \phi, t)$ as an additional dependent variable, as well as a new timescale τ_K [see Eq. (68)] that reflects the characteristic relaxation time for surface dilatation. We further assume that the (thermodynamic) tension in the surface-viscous domain is approximately equal to the static tension,

$$\gamma \approx \gamma_0, \tag{D1}$$

which eliminates the need for an additional equation of state relating γ and ρ_s. In other words, the approximation given by Eq. (D1) neglects the Marangoni effect—the thermodynamic tendency of surface tension to change in response to a change in the surface mass density. Since γ is taken to be a constant, the areal stress admits a purely viscous response to the dynamic pressure oscillation prescribed by Eq. (15).

Under conditions of axial symmetry and time-harmonic linear response, the surface mass density can be expressed in a form similar to Eqs. (17)–(20),

$$\rho_s(\theta, t) = \rho_0 + \delta\rho(\theta) e^{i\omega t}, \tag{D2}$$

where ρ_0 is the initial density and $\delta\rho$ is the linear perturbation amplitude. We render the density perturbation dimensionless as $\delta\bar{\rho} = \delta\rho/\rho_0$ and define two Peclet numbers for surface shear and dilatation:

$$\mathrm{Pe}_\eta = \frac{4\omega\eta_s}{\gamma_0}, \quad \mathrm{Pe}_\kappa = \frac{4\omega\kappa_s}{\gamma_0}. \tag{D3}$$

The governing equations conserving surface mass and momentum [Eqs. (21)–(23)] are then replaced by

$$\frac{d^2\delta\bar{R}}{d\theta^2} + \cot\theta \frac{d\delta\bar{R}}{d\theta} + 2\delta\bar{R} + \frac{i\mathrm{Pe}_\kappa}{2}\delta\bar{\rho} = -2\delta\bar{p}, \tag{D4}$$

$$\frac{d\delta\bar{v}_\theta}{d\theta} + \delta\bar{v}_\theta \cot\theta + 2\delta\bar{R} + \delta\bar{\rho} = 0, \tag{D5}$$

$$\frac{d^2\delta\bar{v}_\theta}{d\theta^2} + \cot\theta \frac{d\delta\bar{v}_\theta}{d\theta} + (1 - \cot^2\theta)\delta\bar{v}_\theta - \frac{\mathrm{Pe}_\kappa}{\mathrm{Pe}_\eta}\frac{d\delta\bar{\rho}}{d\theta} = 0. \tag{D6}$$

The boundary and integral conditions [Eqs. (24)–(28)] are similarly replaced by

$$\delta\bar{v}_\theta = 0, \quad \frac{d\delta\bar{\rho}}{d\theta} = 0, \quad \frac{d\delta\bar{R}}{d\theta} = 0 \quad \text{at} \quad \theta = 0, \tag{D7}$$

$$\frac{d\delta\bar{R}}{d\theta} = 0, \quad \frac{d\delta\bar{v}_\theta}{d\theta} - \delta\bar{v}_\theta \cot\theta - \frac{\mathrm{Pe}_\kappa}{\mathrm{Pe}_\eta}\delta\bar{\rho} = 0 \quad \text{at} \quad \theta = \alpha_0, \tag{D8}$$

$$\delta\bar{v}_\theta = \delta\alpha \quad \text{at} \quad \theta = \alpha_0, \tag{D9}$$

$$\int_0^{\alpha_0} (2\delta\bar{R} + \delta\bar{\rho}) \sin\theta \, d\theta + \delta\alpha \sin\alpha_0 = 0, \tag{D10}$$

$$\delta\bar{R} = -\delta\bar{p} \quad \text{at} \quad \theta = \alpha_0. \tag{D11}$$

Equations (D4)–(D11) comprise a new boundary-value problem for the response functions $\delta\bar{v}_\theta(\theta)$, $\delta\bar{R}(\theta)$, and $\delta\bar{\rho}(\theta)$. Taking the limit as $\mathrm{Pe}_\kappa \to \infty$ while keeping

$$\delta\bar{\gamma} = -\frac{i\mathrm{Pe}_\kappa}{4}\delta\bar{\rho} \tag{D12}$$

finite reduces these equations to the original boundary-value problem given by Eqs. (21)–(28).

Following a similar set of algebraic steps as in Appendix A, Eqs. (D4)–(D6) may be combined to eliminate $\delta\bar{v}_\theta$ and $\delta\bar{R}$ and yield a master equation for the density perturbation $\delta\bar{\rho}$:

$$\left(\frac{1}{i\mathrm{Pe}_\kappa} + \frac{1}{i\mathrm{Pe}_\eta}\right)\frac{1}{\sin\theta}\frac{d}{d\theta}\left(\sin\theta\frac{d\delta\bar{\rho}}{d\theta}\right) - \left(1 - \frac{2}{i\mathrm{Pe}_\kappa}\right)\delta\bar{\rho} = \frac{4}{i\mathrm{Pe}_\kappa}\delta\bar{p}. \tag{D13}$$

This equation has the form of a one-dimensional diffusion-reaction equation in the frequency domain. It is analogous to the surface diffusion equation [Eq. (9)] previously derived for the surface tension in the incompressible limit. Significantly, the first (diffusive) term on the left-hand side of

Eq. (D13) motivates the definition of an *effective* Peclet number,

$$\mathrm{Pe} = \frac{1}{\mathrm{Pe}_\kappa^{-1} + \mathrm{Pe}_\eta^{-1}} = \frac{4\omega\kappa_\mathrm{s}\eta_\mathrm{s}}{\gamma_0(\kappa_\mathrm{s}+\eta_\mathrm{s})} \equiv \frac{\omega R_0^2}{D}, \tag{D14}$$

where

$$D = \frac{\gamma_0 R_0^2(\kappa_\mathrm{s}+\eta_\mathrm{s})}{4\kappa_\mathrm{s}\eta_\mathrm{s}} \tag{D15}$$

is a new diffusion coefficient. Comparing Eqs. (D15) and (11) reveals that the viscous coefficient $4\eta_\mathrm{s}$ in the denominator has been replaced by $4\kappa_\mathrm{s}\eta_\mathrm{s}/(\kappa_\mathrm{s}+\eta_\mathrm{s})$. The latter quantity is equivalent to the Young's viscosity of thin, continuum sheets.

In Sec. III A, solutions of the one-dimensional boundary-value problem were analyzed in various limits of the Peclet number. In a similar way, several important limits of Eqs. (D4)–(D11) can be deduced in terms of Pe_η and Pe_κ. For instance, simultaneously taking $\mathrm{Pe}_\kappa \gg 2\pi/\alpha_0^2$ and $\mathrm{Pe}_\eta \ll 2\pi/\alpha_0^2$ recovers our previous asymptotic expansions for a weakly sheared, but incompressible, surface domain [see Eqs. (29)–(31) with $\delta\bar{\gamma}$ given by Eq. (D12)]. Another interesting limit is the one in which resistance to surface dilatation is weak: $\mathrm{Pe}_\kappa \ll 2\pi/\alpha_0^2$ and $\mathrm{Pe}_\eta = O(1)$. This limit admits the following (regular) perturbation series in ascending powers of Pe_κ:

$$\frac{\delta\bar{v}_\theta(\theta)}{\delta\bar{p}} = \frac{3}{2}\left(\frac{(1+\cos\alpha_0)\sin\theta}{1+\cos\alpha_0+\cos^2\alpha_0}\right) + O(\mathrm{Pe}_\kappa), \tag{D16}$$

$$\frac{\delta\bar{p}(\theta)}{\delta\bar{p}} = 2 - 3\left(\frac{(1+\cos\alpha_0)\sin\theta}{1+\cos\alpha_0+\cos^2\alpha_0}\right) + O(\mathrm{Pe}_\kappa), \tag{D17}$$

$$\frac{\delta\bar{R}(\theta)}{\delta\bar{p}} = -1 - \frac{i\mathrm{Pe}_\kappa}{2}\left(\frac{(1+\cos\alpha_0)\cos\alpha_0}{1+\cos\alpha_0+\cos^2\alpha_0}\right)\left[\frac{\cos\theta}{\cos\alpha_0}\ln\left(\frac{1+\cos\theta}{1+\cos\alpha_0}\right) + \frac{\cos\alpha_0-\cos\theta}{1+\cos\alpha_0}\right] + O\left(\mathrm{Pe}_\kappa^2\right). \tag{D18}$$

Thus, an $O(1)$ surface dilatation induces an $O(\mathrm{Pe}_\kappa)$ out-of-phase response to the surface shape. Since the areal strain is $O(1)$ according to Eq. (D17), the (viscous) areal stress must be of $O(\mathrm{Pe}_\kappa)$. Thus, both the small-Pe_κ and small-Pe_η limits give rise to a weakly viscous surface stress response, as expected.

The final limit of interest is one in which both Pe_κ and Pe_η are large: $\mathrm{Pe}_\kappa \gg 2\pi/\alpha_0^2$ and $\mathrm{Pe}_\eta \gg 2\pi/\alpha_0^2$. This is a singular limit and, therefore, requires the application of matched asymptotic expansions. If we define the surface tension perturbation $\delta\bar{\gamma}$ according to Eq. (D12) and treat the effective Peclet number of Eq. (D14) as a large parameter, $\mathrm{Pe} \gg 1$, then the singular perturbation analysis of Eqs. (D4)–(D11) follows exactly that of Appendix B. The resulting expansions for $\delta\bar{v}_\theta$, $\delta\bar{\gamma}$, and $\delta\bar{R}$ are given in the main text [Eqs. (32)–(34)].

The above results for finite surface dilatational viscosity neglect the role of surface dilatational *elasticity*. In surfactant systems, dilatational elasticity generally emerges through the (thermodynamic) Gibbs modulus E_s, which characterizes the strength of Marangoni stresses. Since our model assumes a linear response, elastic effects for both shear and dilatation can be easily incorporated by generalizing the viscous moduli $i\omega\eta_\mathrm{s}$ and $i\omega\kappa_\mathrm{s}$ to their complex-valued analogs, G_s^* and E_s^*, through Pipkin's correspondence principle [91]. In this way, all our preceding results in the linear-response regime can be applied to surface-elastic and viscoelastic domains.

[1] K. Nag, J. Pérez-Gil, M. L. F. Ruano, L. A. D. Worthman, J. Stewart, C. Casals, and K. M. W. Keough, Phase transitions in films of lung surfactant at the air-water interface, Biophys. J. **74**, 2983 (1998).

[2] R. H. Notter, *Lung Surfactants: Basic Science and Clinical Applications* (CRC Press, Boca Raton, FL, 2000).
[3] J. A. Zasadzinski, J. Ding, H. E. Warriner, F. Bringezu, and A. J. Waring, The physics and physiology of lung surfactants, Curr. Opin. Colloid Interface Sci. **6**, 506 (2001).
[4] A. N. Thomas and M. A. Borden, Hydrostatic pressurization of lung surfactant microbubbles: observation of a strain-rate dependent elasticity, Langmuir **33**, 13699 (2017).
[5] A. K. Sachan and J. A. Zasadzinski, Interfacial curvature effects on the monolayer morphology and dynamics of a clinical lung surfactant, Proc. Natl. Acad. Sci. USA **115**, E134 (2018).
[6] D. H. Kim, M. J. Costello, P. B. Duncan, and D. Needham, Mechanical properties and microstructure of polycrystalline phospholipid monolayer shells: Novel solid microparticles, Langmuir **19**, 8455 (2003).
[7] P. Marmottant, S. Van Der Meer, M. Emmer, M. Versluis, N. De Jong, S. Hilgenfeldt, and D. Lohse, A model for large amplitude oscillations of coated bubbles accounting for buckling and rupture, J. Acoust. Soc. Am. **118**, 3499 (2005).
[8] K. Ferrara, R. Pollard, and M. Borden, Ultrasound microbubble contrast agents: Fundamentals and application to gene and drug delivery, Annu. Rev. Biomed. Eng. **9**, 415 (2007).
[9] B. Dollet, S. M. van der Meer, V. Garbin, N. de Jong, D. Lohse, and M. Versluis, Nonspherical oscillations of ultrasound contrast agent microbubbles, Ultrasound Med. Biol. **34**, 1465 (2008).
[10] M. Cattaneo and O. Supponen, Shell viscosity estimation of lipid-coated microbubbles, arXiv:2302.06339.
[11] B. A. Camley, C. Esposito, T. Baumgart, and F. L. H. Brown, Lipid bilayer domain fluctuations as a probe of membrane viscosity, Biophys. J. **99**, L44 (2010).
[12] M. Rahimi, A. DeSimone, and M. Arroyo Balaguer, Curved fluid membranes behave laterally as an effective viscoelastic medium, Soft Matter **9**, 11033 (2013).
[13] J. K. Sigurdsson and P. J. Atzberger, Hydrodynamic coupling of particle inclusions embedded in curved lipid bilayer membranes, Soft Matter **12**, 6685 (2016).
[14] D. Andelman, F. Brochard, and J. F. Joanny, Phase transitions in Langmuir monolayers of polar molecules, J. Chem. Phys. **86**, 3673 (1987).
[15] L. S. Hirst, P. Uppamoochikkal, and C. Lor, Phase separation and critical phenomena in biomimetic ternary lipid mixtures, Liq. Cryst. **38**, 1735 (2011).
[16] S. Komura and D. Andelman, Physical aspects of heterogeneities in multi-component lipid membranes, Adv. Colloid Interface Sci. **208**, 34 (2014).
[17] H. E. Gaub and H. M. McConnell, Shear viscosity of monolayers at the air-water interface, J. Phys. Chem. **90**, 6830 (1986).
[18] V. M. Kaganer, H. Möhwald, and P. Dutta, Structure and phase transitions in Langmuir monolayers, Rev. Mod. Phys. **71**, 779 (1999).
[19] J. Ding, H. E. Warriner, and J. A. Zasadzinski, Viscosity of Two-Dimensional Suspensions, Phys. Rev. Lett. **88**, 168102 (2002).
[20] E. Hermans and J. Vermant, Interfacial shear rheology of DPPC under physiologically relevant conditions, Soft Matter **10**, 175 (2014).
[21] A. K. Sachan, S. Q. Choi, K. H. Kim, Q. Tang, L. Hwang, K. Y. C. Lee, T. M. Squires, and J. A. Zasadzinski, Interfacial rheology of coexisting solid and fluid monolayers, Soft Matter **13**, 1481 (2017).
[22] C.-C. Chang, A. Nowbahar, V. Mansard, I. Williams, J. Mecca, A. K. Schmitt, T. H. Kalantar, T.-C. Kuo, and T. M. Squires, Interfacial rheology and heterogeneity of aging asphaltene layers at the water–oil interface, Langmuir **34**, 5409 (2018).
[23] M. Seul and D. Andelman, Domain shapes and patterns: the phenomenology of modulated phases, Science **267**, 476 (1995).
[24] M. J. Boussinesq, The application of the formula for surface viscosity to the surface of a slowly falling droplet in the midst of a large unlimited amount of fluid which is at rest and possesses a smaller specific gravity, Ann. Chim. Phys. **29**, 357 (1913).
[25] L. E. Scriven, Dynamics of a fluid interface equation of motion for newtonian surface fluids, Chem. Eng. Sci. **12**, 98 (1960).

[26] D. A. Edwards, H. Brenner, and D. T. Wasan, *Interfacial Transport Processes and Rheology* (Butterworth-Heinemann, Stonheam, MA, 1991).
[27] T. Verwijlen, P. Moldenaers, H. A. Stone, and J. Vermant, Study of the flow field in the magnetic rod interfacial stress rheometer, Langmuir **27**, 9345 (2011).
[28] G. J. Elfring, L. G. Leal, and T. M. Squires, Surface viscosity and marangoni stresses at surfactant laden interfaces, J. Fluid Mech. **792**, 712 (2016).
[29] M. S. Bhamla, C. Chai, M. A. Alvarez-Valenzuela, J. Tajuelo, and G. G. Fuller, Interfacial mechanisms for stability of surfactant-laden films, PloS one **12**, e0175753 (2017).
[30] H. Manikantan, Tunable Collective Dynamics of Active Inclusions in Viscous Membranes, Phys. Rev. Lett. **125**, 268101 (2020).
[31] M. L. Henle and A. J. Levine, Hydrodynamics in curved membranes: The effect of geometry on particulate mobility, Phys. Rev. E **81**, 011905 (2010).
[32] F. Quemeneur, J. K. Sigurdsson, M. Renner, P. J. Atzberger, P. Bassereau, and D. Lacoste, Shape matters in protein mobility within membranes, Proc. Natl. Acad. Sci. USA **111**, 5083 (2014).
[33] N. Singh and V. Narsimhan, Impact of surface viscosity on the stability of a droplet translating through a stagnant fluid, J. Fluid Mech. **927**, A44 (2021).
[34] P. Gera and D. Salac, Modeling of multicomponent three-dimensional vesicles, Comput. Fluids **172**, 362 (2018).
[35] P. Gera and D. Salac, Three-dimensional multicomponent vesicles: Dynamics and influence of material properties, Soft Matter **14**, 7690 (2018).
[36] E. Kreyszig, *Differential Geometry* (University of Toronto Press, Toronto, Canada, 1959).
[37] G. G. Fuller and J. Vermant, Complex fluid-fluid interfaces: Rheology and structure, Annu. Rev. Chem. Biomol. Eng. **3**, 519 (2012).
[38] W. Shi, M. Moradi, and E. Nazockdast, Hydrodynamics of a single filament moving in a spherical membrane, Phys. Rev. Fluids **7**, 084004 (2022).
[39] T. Verwijlen, D. L. Leiske, P. Moldenaers, J. Vermant, and G. G. Fuller, Extensional rheometry at interfaces: Analysis of the cambridge interfacial tensiometer, J. Rheol. **56**, 1225 (2012).
[40] H. Manikantan and T. M. Squires, Surfactant dynamics: Hidden variables controlling fluid flows, J. Fluid Mech. **892**, P1 (2020).
[41] H. A. Stone and L. G. Leal, The effects of surfactants on drop deformation and breakup, J. Fluid Mech. **220**, 161 (1990).
[42] M. Vignes-Adler and H. Brenner, A micromechanical derivation of the differential equations of interfacial statics. iii. line tension, J. Colloid Interface Sci. **103**, 11 (1985).
[43] R. Bulirsch and J. Stoer, *Introduction to Numerical Analysis* (Springer, New York, NY, 2002), Vol. 3.
[44] J. D. Buckmaster, A. Nachman, and L. Ting, The buckling and stretching of a viscida, J. Fluid Mech. **69**, 1 (1975).
[45] T. B. Benjamin and T. Mullin, Buckling instabilities in layers of viscous liquid subjected to shearing, J. Fluid Mech. **195**, 523 (1988).
[46] P. D. Howell, Models for thin viscous sheets, Eur. J. Appl. Math. **7**, 321 (1996).
[47] M. Skorobogatiy and L. Mahadevan, Folding of viscous sheets and filaments, Europhys. Lett. **52**, 532 (2000).
[48] E. Cerda and L. Mahadevan, Geometry and Physics of Wrinkling, Phys. Rev. Lett. **90**, 074302 (2003).
[49] J. D. Paulsen, E. Hohlfeld, H. King, J. Huang, Z. Qiu, T. P. Russell, N. Menon, D. Vella, and B. Davidovitch, Curvature-induced stiffness and the spatial variation of wavelength in wrinkled sheets, Proc. Natl. Acad. Sci. USA **113**, 1144 (2016).
[50] C. M. Bender and S. A. Orszag, *Advanced Mathematical Methods for Scientists and Engineers* (McGraw-Hill, Singapore, 1978).
[51] P. G. Drazin and W. H. Reid, *Hydrodynamic Stability* (Cambridge University Press, Cambridge, UK, 2004).
[52] P. G. Saffman and G. I. Taylor, The penetration of a fluid into a porous medium or Hele-Shaw cell containing a more viscous liquid, Proc. R. Soc. London A **245**, 312 (1958).

[53] J. W. McLean and P. G. Saffman, The effect of surface tension on the shape of fingers in a Hele-Shaw cell, J. Fluid Mech. **102**, 455 (1981).
[54] L. Paterson, Radial fingering in a Hele-Shaw cell, J. Fluid Mech. **113**, 513 (1981).
[55] C.-W. Park and G. M. Homsy, Two-phase displacement in Hele-Shaw cells: Theory, J. Fluid Mech. **139**, 291 (1984).
[56] C.-W. Park and G. M. Homsy, The instability of long fingers in Hele-Shaw flows, Phys. Fluids **28**, 1583 (1985).
[57] P. Muller and F. Gallet, First Measurement of the Liquid-Solid Line Energy in a Langmuir Monolayer, Phys. Rev. Lett. **67**, 1106 (1991).
[58] D. J. Benvegnu and H. M. McConnell, Line tension between liquid domains in lipid monolayers, J. Phys. Chem. **96**, 6820 (1992).
[59] S. Rivière, S. Hénon, J. Meunier, G. Albrecht, M. M. Boissonnade, and A. Baszkin, Electrostatic Pressure and Line Tension in a Langmuir Monolayer, Phys. Rev. Lett. **75**, 2506 (1995).
[60] S. Wurlitzer, P. Steffen, and Th. M. Fischer, Line tension of Langmuir monolayer phase boundaries determined with optical tweezers, J. Chem. Phys. **112**, 5915 (2000).
[61] S. Wurlitzer, P. Steffen, M. Wurlitzer, Z. Khattari, and Th. M. Fischer, Line tension in Langmuir monolayers probed by point forces, J. Chem. Phys. **113**, 3822 (2000).
[62] P. Heinig, P. Steffen, S. Wurlitzer, and Th. M. Fischer, Two-dimensional pendant droplet tensiometry in a Langmuir monolayer, Langmuir **17**, 6633 (2001).
[63] C. W. McConlogue and T. K. Vanderlick, A close look at domain formation in dppc monolayers, Langmuir **13**, 7158 (1997).
[64] D. W. Lee, Y. Min, P. Dhar, A. Ramachandran, J. N. Israelachvili, and J. A. Zasadzinski, Relating domain size distribution to line tension and molecular dipole density in model cytoplasmic myelin lipid monolayers, Proc. Natl. Acad. Sci. USA **108**, 9425 (2011).
[65] N. J. Alvarez, L. M. Walker, and S. L. Anna, A microtensiometer to probe the effect of radius of curvature on surfactant transport to a spherical interface, Langmuir **26**, 13310 (2010).
[66] N. J. Alvarez, L. M. Walker, and S. L. Anna, Diffusion-limited adsorption to a spherical geometry: The impact of curvature and competitive time scales, Phys. Rev. E **82**, 011604 (2010).
[67] N. J. Alvarez, W. Lee, L. M. Walker, and S. L. Anna, The effect of alkane tail length of CiE8 surfactants on transport to the silicone oil–water interface, J. Colloid Interface Sci. **355**, 231 (2011).
[68] N. J. Alvarez, S. L. Anna, T. Saigal, R. D. Tilton, and L. M. Walker, Interfacial dynamics and rheology of polymer-grafted nanoparticles at air–water and xylene–water interfaces, Langmuir **28**, 8052 (2012).
[69] M. D. Reichert, N. J. Alvarez, C. F. Brooks, A. M. Grillet, L. A. Mondy, S. L. Anna, and L. M. Walker, The importance of experimental design on measurement of dynamic interfacial tension and interfacial rheology in diffusion-limited surfactant systems, Colloids Surf. A **467**, 135 (2015).
[70] M. D. Reichert and L. M. Walker, Coalescence behavior of oil droplets coated in irreversibly-adsorbed surfactant layers, J. Colloid Interface Sci. **449**, 480 (2015).
[71] M. L. Davidson and L. M. Walker, Interfacial properties of polyelectrolyte–surfactant aggregates at air/water interfaces, Langmuir **34**, 12906 (2018).
[72] S. Barman, M. L. Davidson, L. M. Walker, S. L. Anna, and J. A. Zasadzinski, Inflammation product effects on dilatational mechanics can trigger the laplace instability and acute respiratory distress syndrome, Soft Matter **16**, 6890 (2020).
[73] S. Narayan, S. Barman, D. B. Moravec, B. G. Hauser, A. J. Dallas, J. A. Zasadzinski, and C. S. Dutcher, Dilatational rheology of water-in-diesel fuel interfaces: Effect of surfactant concentration and bulk-to-interface exchange, Soft Matter **17**, 4751 (2021).
[74] S. V. Iasella, S. Barman, C. Ciutara, B. Huang, M. L. Davidson, and J. A. Zasadzinski, Microtensiometer for confocal microscopy visualization of dynamic interfaces, J. Vis. Exp. **187**, e64110 (2022).
[75] C. O. Ciutara, S. Barman, S. Iasella, B. Huang, and J. A. Zasadzinski, Dilatational and shear rheology of soluble and insoluble monolayers with a Langmuir trough, J. Colloid Interface Sci. **629**, 125 (2023).
[76] R. Bruinsma, F. Rondelez, and A. Levine, Flow-controlled growth in Langmuir monolayers, Eur. Phys. J. E **6**, 191 (2001).

[77] A. Miller and H. Möhwald, Diffusion limited growth of crystalline domains in phospholipid monolayers, J. Chem. Phys. **86**, 4258 (1987).
[78] A. Flores, E. Corvera-Poire, C. Garza, and R. Castillo, Pattern formation and morphology evolution in Langmuir monolayers, J. Phys. Chem. B **110**, 4824 (2006).
[79] A. Flores, E. Corvera-Poiré, C. Garza, and R. Castillo, Growth and morphology in Langmuir monolayers, Europhys. Lett. **74**, 799 (2006).
[80] L. R. Arriaga, I. López-Montero, J. Ignés-Mullol, and F. Monroy, Domain-growth kinetic origin of nonhorizontal phase coexistence plateaux in Langmuir monolayers: compression rigidity of a raft-like lipid distribution, J. Phys. Chem. B **114**, 4509 (2010).
[81] J. Dreier, J. Brewer, and A. C. Simonsen, Texture defects in lipid membrane domains, Soft Matter **8**, 4894 (2012).
[82] C. Valtierrez-Gaytan, J. M. Barakat, M. Kohler, K. Kieu, B. L. Stottrup, and J. A. Zasadzinski, Spontaneous evolution of equilibrium morphology in phospholipid-cholesterol monolayers, Sci. Adv. **8**, eabl9152 (2022).
[83] S. R. Coriell and R. L. Parker, Stability of the shape of a solid cylinder growing in a diffusion field, J. Appl. Phys. **36**, 632 (1965).
[84] H. M. McConnell and V. T. Moy, Shapes of finite two-dimensional lipid domains, J. Phys. Chem. **92**, 4520 (1988).
[85] H. M. McConnell, Theory of hexagonal and stripe phases in monolayers, Proc. Natl. Acad. Sci. USA **86**, 3452 (1989).
[86] D. J. Benvegnu and H. M. McConnell, Surface dipole densities in lipid monolayers, J. Phys. Chem. **97**, 6686 (1993).
[87] H. M. McConnell, Harmonic shape transitions in lipid monolayer domains, J. Phys. Chem. **94**, 4728 (1990).
[88] J. M. Barakat and T. M. Squires, Shape morphology of dipolar domains in planar and spherical monolayers, J. Chem. Phys. **152**, 234701 (2020).
[89] K. Masschaele, J. Fransaer, and J. Vermant, Direct visualization of yielding in model two-dimensional colloidal gels subjected to shear flow, J. Rheol. **53**, 1437 (2009).
[90] I. Williams, J. A. Zasadzinski, and T. M. Squires, Interfacial rheology and direct imaging reveal domain-templated network formation in phospholipid monolayers penetrated by fibrinogen, Soft Matter **15**, 9076 (2019).
[91] A. C. Pipkin, *Lectures on Viscoelasticity Theory*, 2nd ed. (Springer, New York, NY, 1986).
[92] M. van Dyke, *Perturbation Methods in Fluid Mechanics* (The Parabolic Press, Stanford, CA, 1975).
[93] E. W. Hobson, *The Theory of Spherical and Ellipsoidal Harmonics* (Cambridge University Press, Cambridge, UK, 1931), p. 117.